Enhancing the Performance of Shape-controlled Octahedral Rhodium Doped PtNi Nanoalloys inside Hydrogen-air Fuel Cell Cathodes Using a Rational Design of Catalysts, Supports and Layering

L. Pan,[1] A. Parnière,[2] O. Dunseath,[3] D. Fongalland,[3] G. Nicolau,[3] C. C. Weber,[1] J. Lu,[1] M. Klingenhof,[1] A. Arinchtein,[1] H.-S. Oh,[4] P.-Y. Blanchard,[2] S. Cavaliere,[2,5] M. Heggen,[6] R. E. Dunin-Borkowski,[6] A. Martinez Bonastre,[3] F. Dionigi,[1] J. Sharman,[3] D. Jones[2] and P. Strasser[1]**

[1] Technische Universität Berlin, Straße des 17. Juni 124 – 10623, Berlin – Germany.

[2] ICGM, Univ. Montpellier, CNRS, ENSCM, 34095 Montpellier cedex 5, France.

[3] Johnson Matthey Technology Centre, Blount's Court, Sonning Common, Reading RG4 9NH, United Kingdom

[4]Clean Energy Research Center, Korea Institute of Science and Technology, 02792, Seoul, Republic of Korea.

[5] Institut Universitaire de France (IUF), 1 rue Descartes, 75231 Paris cedex 05, France.

[6] Ernst Ruska-Centre for Microscopy and Spectroscopy with Electrons, Forschungszentrum Jülich GmbH, 52425 Jülich, Germany.

*Corresponding author

Key words: highly loaded octahedral PtNi(Rh), N-doped carbon, stabilization effect, high current density performance, strategies for translation of RDE performance into MEA

Abstract

Octahedral PtNi alloy nanoparticles show very high catalytic activity for the oxygen reduction reaction. However, their integration in membrane electrode assemblies (MEAs) is challenging, resulting in low fuel cell performance. We report the application of three strategies that are promising to improve the MEA-based fuel cell performance of octahedral PtNi alloy nanoparticles: 1) Rh surface doping to stabilize the morphology, 2) high Pt weight percentage loading on carbon to decrease the catalyst layer thickness (at parity of geometric-area-normalized Pt loading), and 3) N functionalized carbon supports to more homogeneously distribute the ionomer. The surface chemistry of the Rh dopants is analysed by *in situ* X-ray absorption spectroscopy (XAS) under applied potentials in liquid half-cell. The Rh dopants are present at the catalyst surface with a local coordination to oxygen atoms as in Rh oxide and show potential dependent changes in oxidation states. A rotating disk electrode (RDE) screening showed advantages in using Ketjen Black EC300-J instead of carbon Vulcan XC72R to accommodate high Pt weight percentage loading (~30 Pt wt%). Finally, a Rh doped PtNi nanoparticle catalyst was grown on 3% nitrogen doped Ketjen Black and tested in MEA-based single cell, after being annealed and acid washed. The results showed modest mass activity (MA), 0.35 A mg_{Pt}^{-1} at 0.9 V, but significantly high performance at high current density for octahedral PtNi nanoparticles, 1500 mA cm^{-2} at 0.6 V, to our knowledge the highest to date for this class of catalysts. Despite this achievement, the full potential of N-doping could not be utilized, with samples showing negligible differences with respect to undoped carbon in both high humidity and low humidity MEA testing. Even though no enhancement of mass transport at high current density by better distribution of the ionomer on the N-doped carbon was seen in MEA, this could be due to the diffusion of Ni cations, affecting ionomer interaction and overwhelming the effect of nitrogen species on the support.

1. Introduction

Using hydrogen as fuel, proton exchange membrane fuel cells (PEMFCs) represent one of the most promising alternative energy conversion devices and a technology intensively explored due to its zero-carbon emission and high energy yield. However, the performance is mainly bottlenecked by the slow kinetics of the oxygen reduction reaction (ORR) at the cathode, where catalysts are subjected to a harsh environment during operation. Platinum, with its high stability and activity, is considered to be the most promising metal and an almost unavoidable component of the PEMFC ORR catalysts[1-6]. Moreover, limited by the high cost and scarce quantity of the noble metal supply, a reduction of Pt usage is essential for PEMFCs towards realizing large-scale commercialization of PEMFC vehicles. To maximize the Pt utilization efficiency, Pt-based catalysts instead of pure platinum catalysts have been considered one of the most potential candidates. [7] One of these strategies is to alloy Pt with other metals to enhance the intrinsic catalytic activity and so reduce the overpotentials for the ORR. Pt alloys range from binary alloys, i.e. PtNi, to high entropy alloys with 5 or more additional metals. [8] Numerous approaches have been discussed to optimize the electronic or surface structure of the nanocatalysts.[6]

Highly active shape-controlled PtNi alloys tune the chemisorption of reactive oxygen intermediates on the catalyst surface through a shift of the Pt electronic d-band center, which is why the $Pt_3Ni(111)$ surface is more active than other Pt_3Ni and pure Pt surface orientations.[9, 10] The design and construction of nanoparticles with an enrichment of (111) facets on the surface could be optimized with morphology-controlled routes and results in octahedral shape. Octahedral nanoparticles made of pure Pt,[11] PtCo[12, 13] and PtNi[14, 15] have been synthesized and their ORR catalytic performance evaluated, with major efforts focused on the more active PtNi compositions. Now, under fuel cell operation conditions the Ni atoms in the nanoparticle surface tend to leach out. This compositional change and the associated morphological degradation cause a decrease of catalytic activity. Furthermore, the generation of Ni cations has a negative influence on the ionomer and the proton exchange membrane, causing loss of cell performance. Therefore, stabilizing the (111) facets and their composition is a key challenge to the translation and validation of the preeminent performance of highly active ORR catalysts from wet cells to fuel cell PEMFC applications. Among the strategies proposed to address this challenge, the addition of a third surface dopant metal such as Mo, Rh, Cu, Ga, Co has shown an enhancement of activity and/or stability over the PtNi/C catalysts in rotating disk electrodes.[12, 14, 16-18] For example, a suppression effect on the Pt diffusion by Rh doping was first reported by Beermann *et al.*,[19] which resulted in exceptional morphological stability in RDE measurements, where the octahedral shape was maintained even past 30,000 potential cycles. However, the performance of Rh doping in a fuel cell and insight in the Rh electronic structure during operation, which is important to further clarify the role that Rh plays on the nanoparticle surface, have remained elusive.

In addition to PtNi octahedra, other nanostructured Pt-based and PtNi catalysts have been proposed that showed exceptional catalytic ORR activity in RDE, such as nanocages and nanowires. However, similarly to the octahedra, MEA-based single cell data are scarcely available, and often showed a much lower enhancement factor vs Pt/C benchmarks, relative

to RDE measurements. The underlying reason has not been fully understood. So far, the factors that would affect the loss of activity are hypothesized to derive from the different conditions in an MEA. Major differences include: i) the working temperature. In MEA testing, it is crucial to operate under elevated temperature, typically 60-80 °C; while it is true that RDE experiments are conventionally conducted at room temperature (RT), to comprehensively assess catalysts' stability, it is important to consider the influence of elevated temperatures and higher upper limit voltages, as these conditions are known to play a significant role in catalyst degradation. While our research primarily focuses on milder test conditions, we acknowledge that many research teams have reported accelerated stress testing (AST) data in liquid cells at elevated temperatures, such as 80°C or at harsher potential ranges. [20-22] ii) the electrolyte: in RDE, conventionally $HClO_4$ or H_2SO_4 aqueous solution are used as electrolyte, but the concentration tends to be low, normally 0.1 M $HClO_4$ or 0.05 M H_2SO_4.[23, 24] In the MEA there is no liquid electrolyte, besides water produced during operation, and protons are transported by the ionomer. Therefore, the acidity in the MEA could be higher than in the liquid cell tests. This high acidity plausibly triggers the leaching of the less noble metal on the surface of the nanoparticles; thus, the morphological benefits may be offset in the resulting catalyst surfaces, which could also result in lowered stability. The leached metal ions may contaminate the ionomer and membrane and block the ion-exchange sites. They have a detrimental role for the ionomer, impacting proton conduction and O_2 transport through the ionomer.[25-28] There is evidence that during MEA measurements, metal ions leached from the cathode were transported to the anodic side across the membrane. iii) the ionomer content: as mentioned above, the ionomer content could be higher than standard RDE inks (higher ionomer/carbon ratio), and the interaction of the ionomer with the catalyst surface could cause the poisoning effect of the catalysts.

Today's state-of-the-art (SoA) mass activity performance of doped PtNi octahedral nanoparticles in MEA-based single cell measurements is 0.45 A mg_{Pt}^{-1} at 0.9 V in hydrogen-oxygen feed.[29] While this was the highest reported activity in MEA-based single cell for this type of shaped catalyst, the enhancement factor vs shape-unselective Pt/C was much lower than the 10x factor projected earlier based on liquid RDE cell screenings, but was close to what was reported for optimized PtCo on high surface carbons (*i.e.* 0.6 A mg_{Pt}^{-1} at 0.9 V). Furthermore, the performance in hydrogen-air at 0.6 V was only 1170 mA cm^{-2}_{geo} (corresponding to a power density of 0.70 W cm^{-2}), which is lower than the values obtained and reported with SoA non-shape selective (cuboctahedral) PtCo and PtNi catalysts (power densities ~> 1 W cm^{-2}). Clearly, this performance gap between SoA catalysts and octahedral PtNi catalysts under hydrogen-air operation needs to be addressed and overcome to make these family of catalysts competitive and suitable for application in commercial PEMFCs.

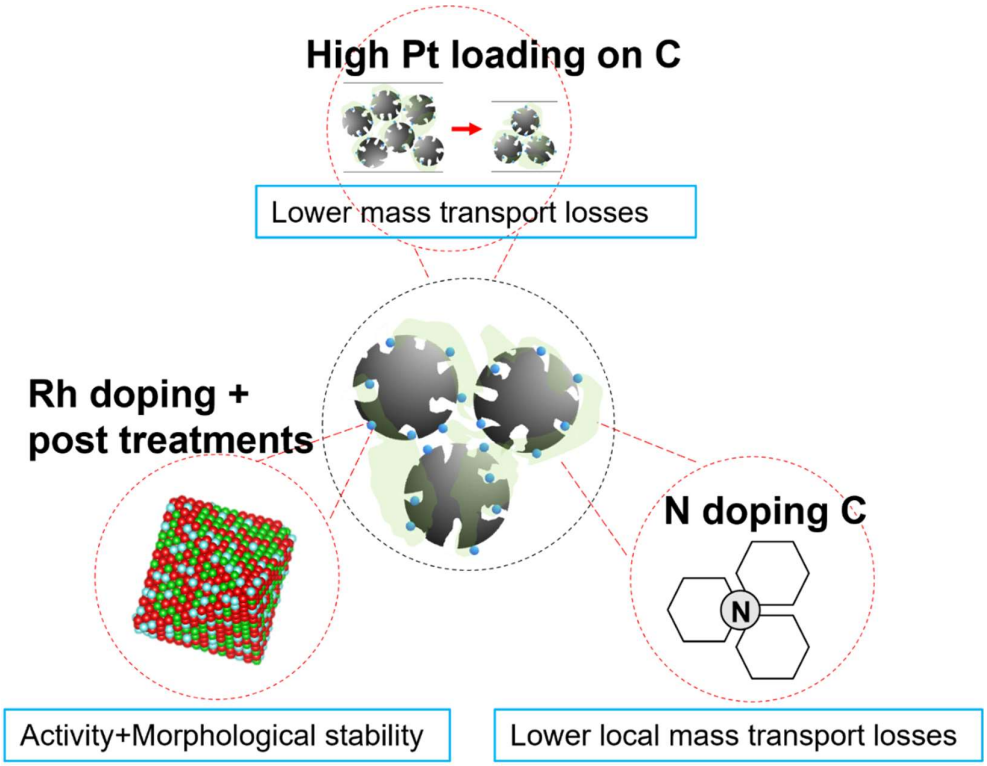

Figure 1. Schematic illustration of the strategies to improve MEA performance of PtNi octahedra. The approaches including doping with a third metal, Rh, to improve the morphological stability and intrinsic activity, reducing cathode catalyst layer thickness by increasing the Pt loading, and N-functionalization of the carbon support to optimize the ionomer distribution.

In this work, we demonstrate how the MEA performance gap of octahedrally shaped doped PtNi can be overcome by the combination of three materials design strategies, (Fig.1). First, we addressed the challenge related to morphological stability by introducing a Rh-based dopant on the surface, which resulted in a great increase in stability in RDE, as the first step to improve MEA performance. This was combined with post-treatments of the upscaled catalysts, including heating-annealing and acid-leaching, to optimize the surface composition and further reduce Ni leaching in the following MEA tests. Second, we tuned the composition of the catalyst layer to modify its thickness and behavior. It is known that the PGM loading at the cathode catalyst layer has an impact on the cell performance.[30] In particular, the thickness of the cathode catalyst layer and local transport behavior are the consequential significant parameters. In aiming to lower the mass transport losses in the layers in MEA tests, attempts in synthesizing PtNi(Rh) NPs with higher Pt wt% loading on carbon have been made, which resulted in thinner cathode layers at parity of cathode loading. Finally, we modified the surface of the carbon support, to improve the ionomer distribution. Studies have shown that carbon support with surface modified carbons, which have N positively charged functional groups reinforced the interaction of the supports with the negatively charged ionomer functional groups ($–SO_3^-$).[31] This further realized better distribution of the ionomer on the

support, hence a better proton accessibility, especially in lower humidity operation condition.[32, 33] We note that this effect has been demonstrated with pure Pt catalysts only, but at the present understanding, it should be transferable also to other catalysts, such as Pt alloys and shaped controlled catalysts. With these hypotheses and following these strategies, we rationally carried out the catalyst, support and catalyst layer design, which resulted in a new state-of-the-art performance in hydrogen-air for octahedral PtNi NPs of 1500 mA cm^{-2} at 0.6 V (0.90 W cm^{-2}), promising for PEMFC applications.

2. Results and Discussion

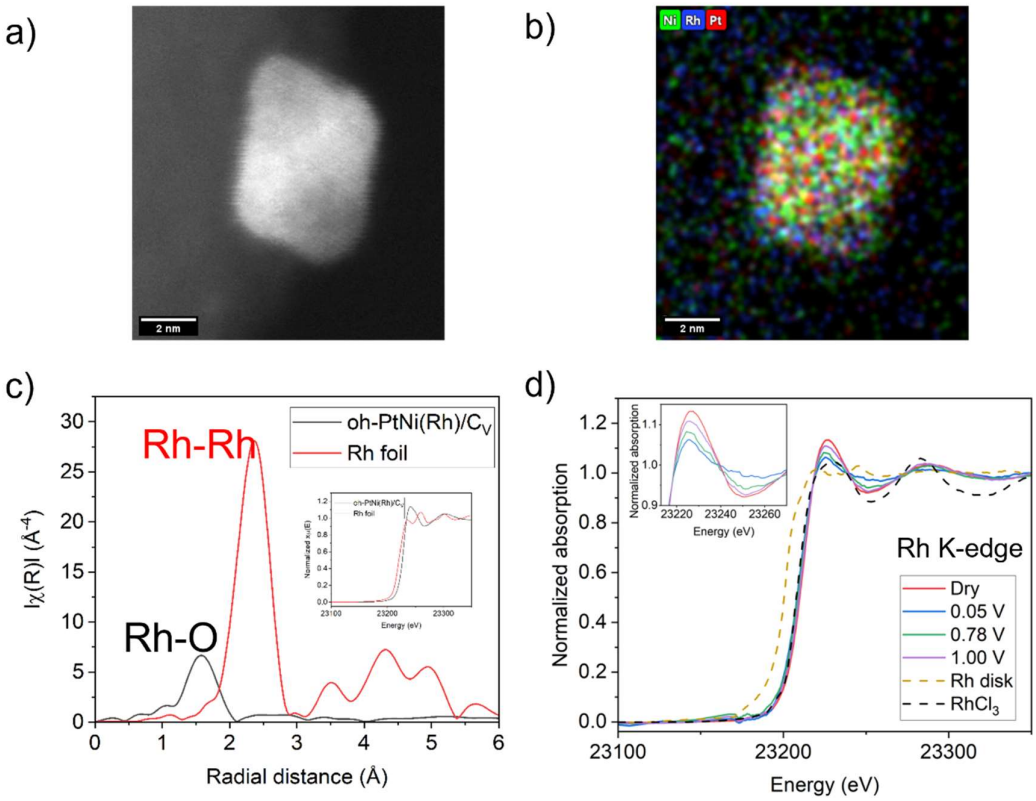

Figure 2. Rh dopant elemental distribution, local and electronic structure. Atomic scale STEM images and results of the *ex situ* and *operando* XAS of Rh in Rh-doped PtNi octahedra sample V19. Intensity-specific a) HAADF-STEM image and b) STEM-EDS map of a single PtNi(Rh) octahedron. c) Fourier-transformed radial distribution functions of ex situ Rh K-edge EXAFS. The oh-PtNi(Rh)/CV sample is compared with Rh foil. d) *operando* XAS characterization of Rh K-edge with applied different potentials alongside with *ex situ* spectra of Rh disk and $RhCl_3$ as reference. The inset shows an enlargement of the white line peaks.

Synthesis of doped octahedral PtNi nanoparticles. Carbon supported, octahedral Rh surface doped PtNi nanoparticles, henceforth referred to as oh-PtNi(Rh), were synthesized using a two-step DMF-based solvothermal synthesis technique as shown in Fig.1. In brief, Pt and Ni precursors and carbon support were mixed and reacted in an autoclave, followed by the addition of Rh precursors and surface doping. One of the resulting Rh-doped PtNi/C catalysts is henceforth referred to as "V19". Its bulk molar composition was $Pt_{64.9}Ni_{33.1}Rh_{2.0}$ and its platinum weight loading is about 20 wt%. Table 1 lists all oh-PtNi(Rh) catalyst materials studied and discussed here with their name and selected properties.

Composition, Chemical State, and Morphology. To understand the role of Rh dopant atoms in the V19 catalyst at an atomic scale, microscopic and spectroscopic characterizations were carried out (Fig. 2 and Fig. S1). The HAADF-STEM image Fig. 2a demonstrates the well-controlled octahedral shape. The microscopic images Fig. 2b show the distribution of the Pt, Ni and Rh atoms at the sub-nanometer scale. Pt and Ni atoms do not appear to follow an anisotropic element distribution, in contrast to larger PtNi nanoparticles.[29, 34] Similarly, Fig. 2b evidence a random distribution of the Rh dopant The EDX single nanoparticle composition was $Pt_{56.6}Ni_{38.8}Rh_{4.6}$, which is close to the $Pt_{64.9}Ni_{33.1}Rh_{2.0}$ average catalyst composition as determined by ICP-OES (a TEM catalyst overview is shown in Supporting Figure S1, while Supporting Figure S2 and S3 show HAADF, three-element and single element maps of the nanoparticle in Fig2, as well as one more nanoparticle).

Operando and *ex situ* electrochemical and synchrotron-based X-ray absorption spectroscopy were collected at the Rh K-edge to explore the chemical state and atomic structure of PtNi(Rh). The sample was measured as dry sample, and with electrolyte at various applied electrode potentials, 0.05 V_{RHE}, 0.78 V_{RHE}, and 1.00 V_{RHE}. This choice covering the potential range typically investigated by LSV in RDE experiments was motivated by the Rh Pourbaix diagram. Rh foil, Rh disk and $RhCl_3$ served as references. The inset of the Fig. 2c compares the X-ray absorption near edge structure (XANES) profiles of oh-PtNi(Rh) and Rh foil for the Rh K-edge (see Supporting Figure S4 for the Pt L_3-edge and Ni K-edge). The Rh K-edge XANES spectra of oh-PtNi(Rh) shifted to higher energy suggesting Rh in a higher redox state. In line with this, the Fourier transform of the extended X-ray absorption fine structure (FT-EXAFS) in Fig. 2c displays the Rh-Rh scattering peak of metallic Rh foil at around 2.4 Å, while the oh-PtNi(Rh) has a peak appearing at around 1.6 Å, which is attributed to the Rh-O scattering path (see Supporting Figure S5-S8 for further details and Supporting Tables S1-S6 for the fitting of the EXAFS). This result and the strongly suppressed Rh-Rh peak reveal that Rh dopant atoms exist in an oxidic state, suggesting that it is not part of the PtNi metal alloy core, but resides at the nanoparticle surface. This data also agrees fully with the *operando* XAS spectra in Fig. 2d): the edge of the dry PtNi(Rh) sample is shifted relative to that of the Rh disk, and almost overlap with the $RhCl_3$ reference, where Rh is in 3+ oxidation state. This indicates that in the as prepared dry PtNi(Rh) sample, the Rh dopant atoms are not metallic, but most likely present as Rh_2O_3 clusters. The white line intensities of the sample that was tested under applied potential in the liquid electrolyte were lower than the dry sample (see inset in Figure 2d and Supporting Figure S7). After exposure to 0.05 V_{RHE}, slight shifts to lower energy and a decrease in white line intensity evidenced that the Rh dopant was reduced at this potential. When the potential shifted to a more anodic value of 0.78 V_{RHE}, trends reversed, i.e. Rh dopant were re-oxidized. This trend continued to 1.0 V_{RHE}. According to the Pourbaix diagram, at 0.78 V_{RHE}, the more thermodynamically stable species that Rh forms should be Rh_2O (from 0.737 V_{RHE}-0.818 V_{RHE}), while at potentials below 0.737 V_{RHE} and above 0.818V Rh metal and Rh_2O_3 should be the more thermodynamically stable species, respectively. Therefore, our selected potential values lay in each of the phase regions of the Pourbaix diagram. While changes in white line intensities were significant, the potential dependent edge energy shifts were small (zoom in Supporting Figure S7). The edge did never fully reach the metallic reference at 0.05 V_{RHE} in our experiments, and so it remains difficult to accurately establish which solid phases

are present in our experiments at the chosen potentials. This is because Rh centers that do not participate in the redox processes, would still contribute to the XAS signal. Also, kinetic barriers might prevent formation of the thermodynamically most stable phases. Nonetheless, our data clearly show that our sample contains redox active Rh species, thus confirming their intended location at the surface of the nanoparticles. Above 0.78 V_{RHE} (probably already above 0.737 V_{RHE}) Rh centers are present as metallic oxide clusters. This insight is important as it helps rationalize the Rh stabilization mechanism.[19] Interestingly, Mo clusters in Mo surface doped PtNi octahedra, were present as surface oxides, not as, rather than in a metallic state.[35] This might suggest that a similar charge transfer stabilization mechanism, based on electron transfer from Pt to surface dopant oxides, operates for either catalyst. Theoretical calculations would be useful to confirm or discard this hypothesis.

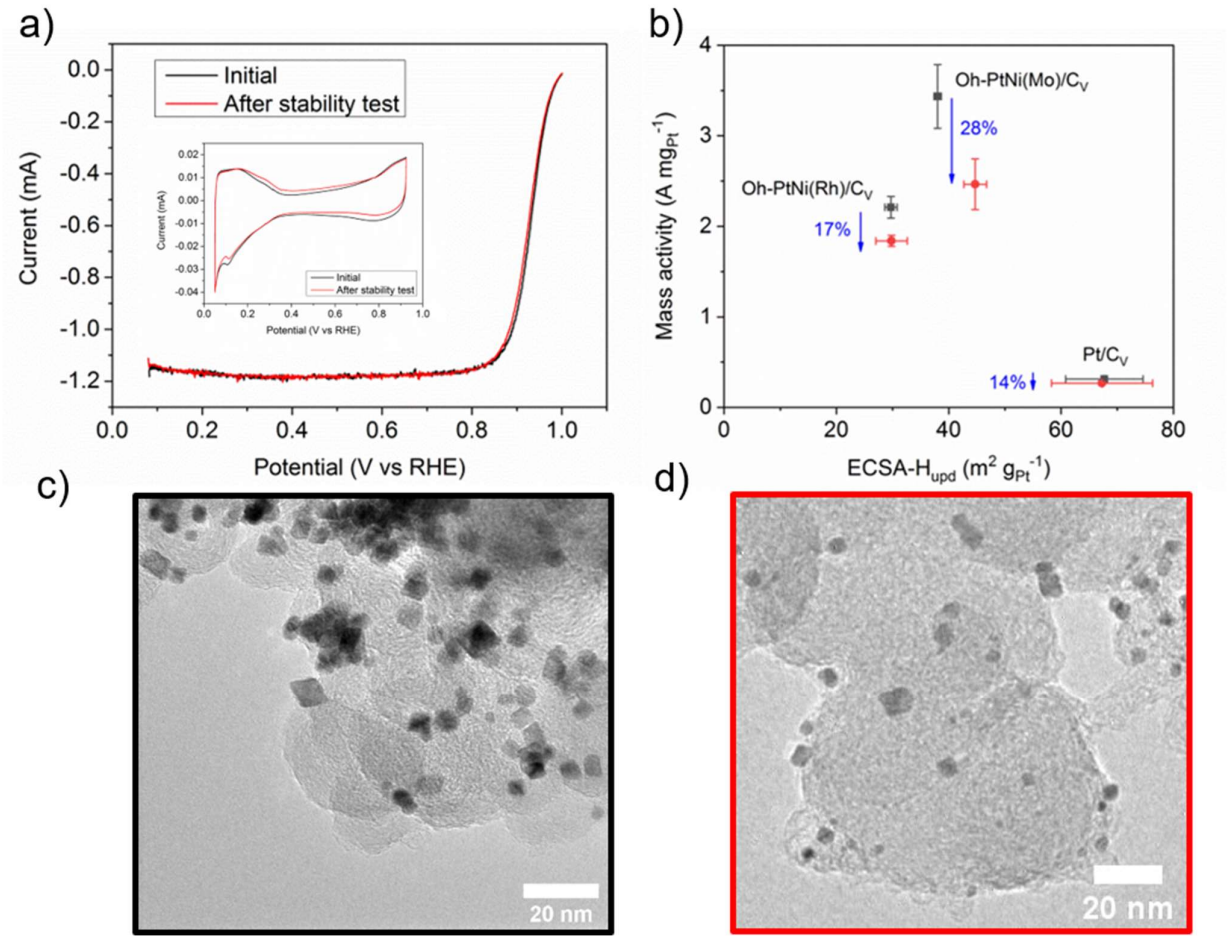

Figure 3. ORR activity and stability of PtNi(Rh)/C_V in RDE. a) Cyclic voltammetry (in the inset) and linear sweeping voltammetry of Rh-doped PtNi octahedra sample V-19, both before (black line) and after the stability test (red line). Both CV and LSV were obtained at 20 mV s^{-1} and 0.1 M $HClO_4$ electrolyte. Stability test with 10k cycles at 100 mV s^{-1} from 0.6 V_{RHE} to 0.925 V_{RHE}. b) Comparison of RDE MA and H_{upd}-ECSA between Mo- and Rh-doped PtNi octahedra and commercial Pt/C. c) and d) TEM images of this sample, before (black frame) and after AST (red frame), respectively.

Electrochemical activity and stability. To study the influence of Rh doping on catalyst activity and stability in the V-19 catalyst, electrochemical voltammetry and microscopy were combined. Both techniques suggested a significant promotion in catalyst stability compared to PtNiMo. Fig. 3a contrasts the initial electrocatalytic oxygen reduction reaction performance of the V-19 catalyst with that after an accelerated stressed test. The polarization curves showed little difference. Similarly, in the inset of Fig. 3a, minor changes are discernible in the catalyst surface cyclic voltammetry (CV) in oxygen-free electrolyte before and after AST. Fig. 3b compares RDE mass activity (at 0.9 V_{RHE}) and H_{upd}-electrochemical surface area (ECSA) of i) Rh-doped PtNi octahedra V19 and ii) Mo-doped PtNi octahedra[29] with similar element composition, type of carbon and Pt loading, $Pt_{66.6}Ni_{31.9}Mo_{1.5}$ and 17.9 Pt wt%, and iii) a commercial Pt/C catalyst. Despite slightly lower absolute mass activity of PtNi(Rh) is slightly lower than Mo, its activity loss is reduced from 28 % loss for Mo to 17 % for Rh, becoming comparable to pure Pt/C (14%). To elucidate the origin of the stability enhancement further, particle morphologies were examined. TEM images in Fig. 3 c,d, evidence sustained octahedral shapes of NPs after the stability test. This suggests a relationship between the electrochemical stability enhancement and Rh doped particle morphology. The observed variations in particle size and structure in Figure 3d after AST can be attributed to the dynamic nature of the catalytic processes and environmental conditions during the testing. During AST, nanoparticles are subjected to harsh conditions such as potential cycling, and chemical exposure, which can lead to the coalescence and growth of some neighboring particles, resulting in the larger-sized particles observed.

Table 1. ICP-OES and overview of oh-PtNi(Rh) catalysts on C_V and C_{KB} and at normal and high loading.

Sample label	Carbon	Target loading (Ptwt%)	Actual loading (Ptwt%)	Atomic composition
V-19	Vulcan XC72R	20	19.3	$Pt_{64.9}Ni_{33.1}Rh_{2.0}$
V-35	Vulcan XC72R	40	34.6	$Pt_{64.5}Ni_{31.9}Rh_{3.6}$
KB-20	Ketjen Black EC-300J	20	20.0	$Pt_{68.7}Ni_{30.9}Rh_{0.4}$
KB31	Ketjen Black EC-300J	40	30.5	$Pt_{63.0}Ni_{32.6}Rh_{4.4}$

Motivated by the stabilization effect observed in liquid electrolyte RDE tests, a series of additional catalysts were prepared with varying Pt loadings and carbon support types. Catalysts with higher Pt weight loadings with enhanced stability and without compromised catalytic activity are highly attractive, as these would render catalyst layers thinner and more durable at given MEA geometric Pt loadings. Vulcan Cabot XC72R and Ketjen Black EC-300J were selected as carbon supports (table 1). Catalyst labels include the acronyms of the carbon type and the numbers refer to the actual Pt weight loading. Both 20 Pt wt% and 40 Pt wt% catalysts were prepared. Compositions of these four samples were comparable, with all four

catalysts sharing a Pt/Ni ratio around 2. This is important to rule out activity differences due to this parameter.[36]

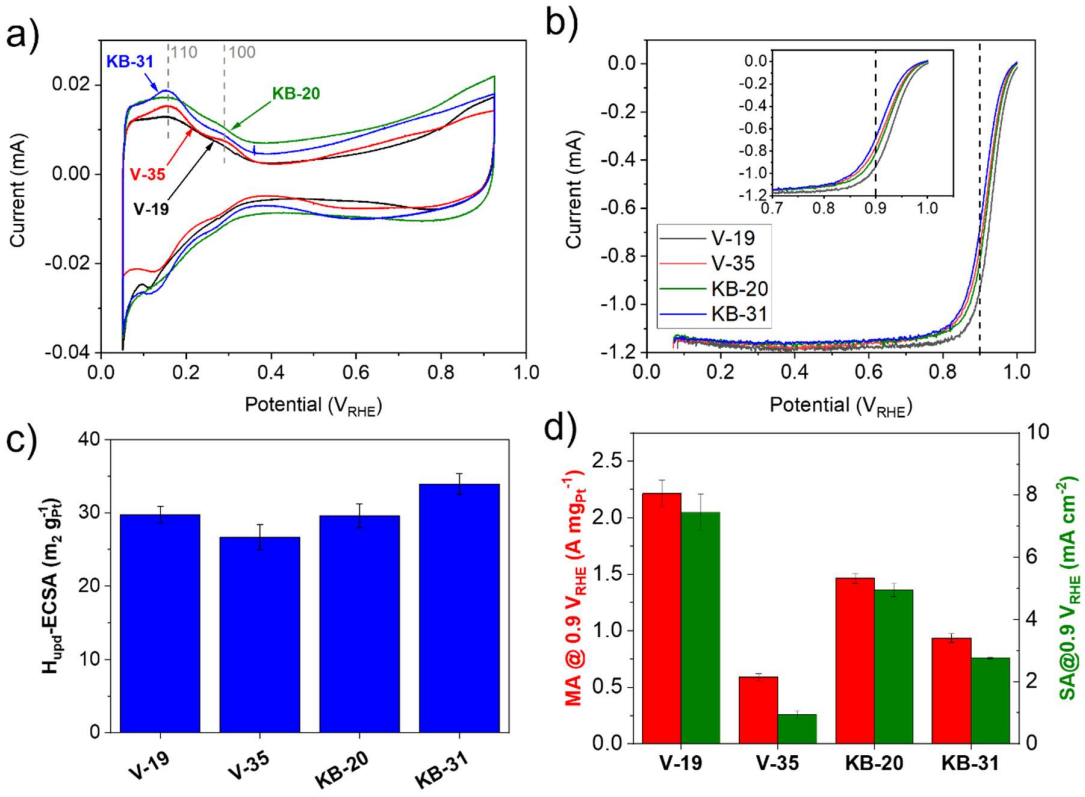

Figure 4. RDE electrochemical performance of Rh doped oh- PtNi(Rh) catalysts of Table 1. a) CV curves of four PtNi(Rh) samples. For the sample V-35, the loading on glassy carbon electrode was roughly twice the others, and therefore the CV is rescaled by half, for better comparison. b) ORR polarization curves. In the inset is a zoom-in plot to verify differences at 0.9 V_{RHE}. Here V-35 is not rescaled. c) Comparison of the H_{upd}-ECSA. d) Comparison of the MA and the SA at 0.9 V_{RHE}.

To investigate the effect of Pt weight loading and carbon support porosity, the RDE ORR performance of all catalysts are compared in Fig. 4. Fig. 4a reveals a similarly lower double layer capacitance of V-19 and V-35 compared to KB-20 and KB-31, in agreement with the higher surface area of this carbon. In general, the CV shape is typical of Pt-based catalyst nanoparticles on carbon support. The peak on the curve occurs around 0.14 V_{RHE} is considered to be the H_{upd} on PtNi(110) and the peak at 0.3 V_{RHE} is related to (100) facets. The plateau shown on V-19 and KB-20 from 0.05 V_{RHE} to 0.14 V_{RHE} may be mainly associated with (111) active facets, plus minor contributions from the other facets. It is worth to note, that the measurement of the V-35 catalyst was performed with twice the regular geometric Pt loading (drop casting of the ink repeated twice) due to the low film quality at regular loading. We believe that the reason for the poor-quality film lies in the insufficient amount of total material deposited in that case, caused by a combination of high Pt wt% and low surface area

of carbon Vulcan, since the same issue was not observed with KB-31. The values of ECSA-H_{upd} (Fig. 4c) are similar, yet there are some significant differences. In particular, V-35 has the lowest ECSA. A possible reason is that the surface area of the solid carbon became limited when the Pt mass loading raised so much, resulting in agglomeration of the nanoparticles (see for comparison the CO stripping in Supporting Figure S9). V-19 and KB-20 exhibited a similar ECSA, while the ECSA of KB-31 is only slightly higher. The reason could lie in a size inhomogeneity or elemental distribution in this sample (see a slight difference in XRD in Supporting Figure S10). To measure the electrochemical ORR activity, linear sweep voltammetry was conducted and the curves for all 4 samples are shown in Fig. 4b and Fig. 4d.

Considering our four samples have similar ECSA-Hupd values, their MA and specific activity (SA) share the same trend in Fig. 4d. The Pt MA of catalyst V-19 of 2.4 A mg_{Pt}^{-1} topped that of V-35, presumably due to higher Pt weight loading and resulting agglomeration. The MA of KB-20 trailed that of V-19, yet achieved 1.5 A mg_{Pt}^{-1}, which ~4-7x more active than Pt/C references. The MA of KB-31 was only ~1.0 A mg_{Pt}^{-1}. The trend among these four samples revealed that lower loaded samples had higher MA than higher loaded catalysts on their corresponding carbons. However, the activity drop with the porous carbon was less than with the solid carbon, and a higher absolute mass activity was reached. Therefore, the porous carbon, and specifically KB-31, was selected as our candidate for thin cathode layers in Membrane Electrode Assembly single fuel cells.

Shape-selective oh-PtNi(Rh) catalyst scale-up on N-doped carbon supports. To translate the favorable RDE Pt MA of the selected oh-PtNi(Rh) from the liquid screening cell into a 50 cm^2 MEA cell environment, the ~100 mg small scale synthesis of KB-31 was first scaled-up to the gram scale. To achieve this, a novel large-scale synthesis protocol was developed. In that protocol, N-doped carbon supports were employed to i) lower the proton transport limitations and ii) to achieve higher cell power density at high current density, thanks to ionomer-interaction effects resulting in a more uniform ionomer distribution. The reason we introduce N-doped carbons at this point is because kinetic effects between N functional groups and the ionomer do not manifest in liquid electrolyte, due to the abundance of protons. Validation requires MEA-based single cell measurements at low relative humidity, as we will discuss in the following. However, a preliminary RDE study in small batches is useful to exclude material combinations or systems that do not satisfy the desired performance criteria, and as a screening purpose. Thus, a preliminary N doping study of a Vulcan carbon was conducted (see Supporting Figures S11-S14), where unsupported shaped Rh-doped oh-PtNiRh octahedral nanoparticles were synthesized in a first step, followed by the addition of the carbon support in a second step. This strategy minimized catalyst composition and morphology effects and allowed focus on support effects. Supporting Figure S12 demonstrates the surface voltammetry and electrocatalytic ORR activity of the N-doped catalysts systems. N-doping from 0, to 0.5 and to 3 wt% raised the ORR activity in RDE experiments, likely thanks to an increase in ECSA, as determined by CO stripping (Supporting Figure S13). This could be explained by a reduction of nanoparticle agglomeration in the presence of N functionality, which was particularly effective at 3 wt%. Therefore, with reasonable guess, the value of 3 wt% was selected and another large batch replica of the KB-

31 oh-PtNi(Rh)/C catalyst with a target loading of 30 Pt wt% supported on 3 wt% N-doped Ketjen Black carbon was prepared.

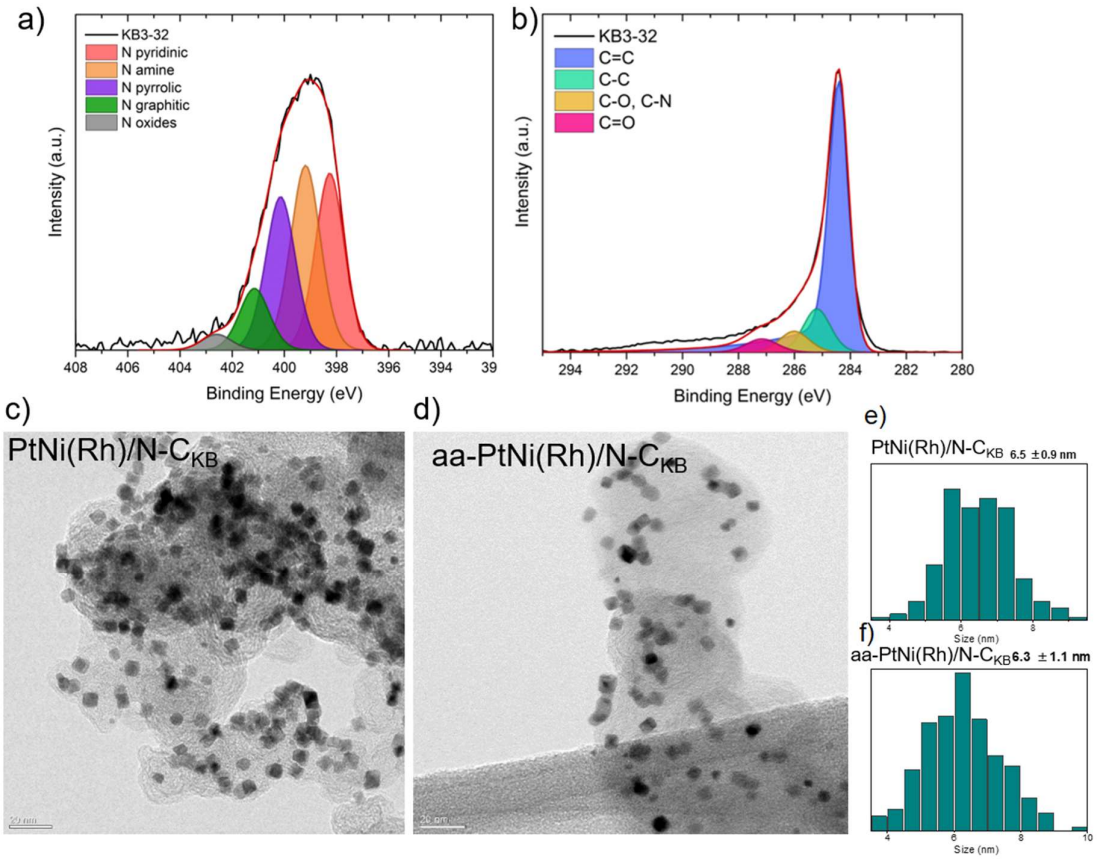

Figure 5: Chemical Analysis of N-doped Ketjen Black carbons. XPS spectra and species assignments in the a) N1s and b) C1s range of the N-doped carbon. c) d) TEM images of oh-PtNi(Rh) on Ketjen Black EC300J carbon with acid-leaching/annealing post-treatment and without, respectively. e,f) Particle size histograms of oh-PtNi(Rh) supported on N-doped Ketjen Black EC300J before e) and after f) the annealing/acid leaching treatment of Figure S18.

A chemical state and N speciation analysis in N-doped carbon was carried out using X-ray photoelectron spectroscopy (XPS). Fig. 5a reports the N 1s region and unveils 5 individual contributions centered at 402.60 eV, 401.15 eV, 400.15 eV, 399.19 eV and 398.26 eV associated with oxidized, graphitic, pyrrolic, amine and pyridinic N, respectively (Table S9, Table S12). The amount of the nitrogen doped into the Ketjen Black carbon was 3.15 wt% and 2.86 wt%, respectively for the 2 batches produced by plasma doping, each 300 mg. The spectra in Fig. 5b shows the C 1s region around 284 eV, where four species resulting from fitting. The main peak at 284.41 eV, indicates a dominant composition of 65.7 at% corresponding to the sp^2 carbon atoms. The other peaks were located at 285.20 eV, 286.01 eV and 287.16 eV, and represented the sp^3 C, C-O together with C-N and C=O groups,

respectively (further details of the XPS analysis in Supporting Tables S9-S10 and Supporting Figure S15).

TEM and ICP-OES compositions of the as-synthesized scaled-up batches of the oh-PtNi(Rh) catalysts supported on the doped and undoped carbon support are compared in Supplementary Figure S16, and their RDE performance in Figure S17 and Table S13. To improve the high current density MEA performance and to avoid Ni-leaching during the cell tests, the as-synthesized scaled-up catalysts underwent an annealing/acid washing procedure, indicated by "aa" (Supporting Figure S18). TEM images confirmed that the octahedral morphology (Fig. 5c,d) as well as the particle size distributions (Fig 5 e,f and Supporting Figure S20) were maintained after the "aa" post treatment. While the ECSAs were similar for both "aa" catalysts, their ORR MA values at 0.9 V_{RHE} decreased with respect to the as-synthesized scaled-up catalysts due to partial particle agglomeration after the thermal treatment and morphological and compositional change after the Ni leaching. In the XRD patterns in Fig. S19 it is shown that the patterns after "aa" procedure become more narrow, this can also be due to the partial agglomeration among nanoparticles. However, the MAs of the two "aa" catalysts (Supporting Figure S21 and Supporting Table S14) as well as their elemental composition (Supporting Figure S18) and phase composition (Supporting Figure S19) were quite comparable, leaving the impact of the N functionalization as the major difference between the batches. Comparison of the N content after "aa" treatments showed only a slight decrease in the N/C ratio (Supporting Figure S22). At a sustained significant level of N-doping (N/C ratio is above 0.015, corresponding to a N wt% of 1.5%). Moreover, we have also conducted RDE stability test under 80 °C with sample aa oh-PtNi(Rh) (Figure S23). As a result, the ECSA has lessened and the limiting current decreased after the AST. While these results seem to suggest instability at high temperature, however, the interpretation of the behavior of PtNi alloy in such condition is limited so far since most of RDE experiments running under 80 degrees were conducted using pure Pt catalysts[20, 22, 37]. Since the behavior in MEA might be different than in liquid electrolyte, we tested our catalyst in MEA.

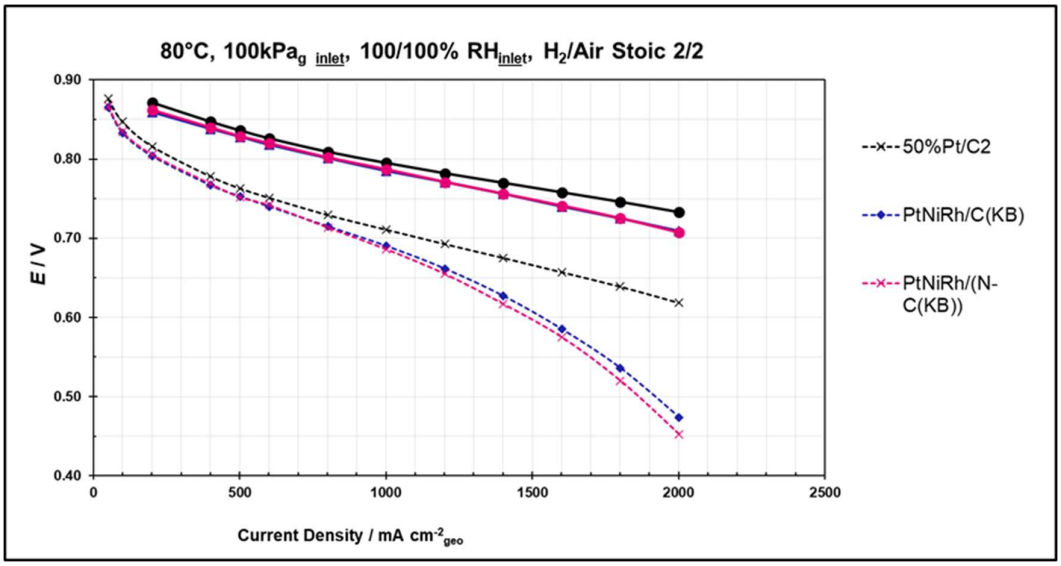

Figure 6. Impact of carbon N doping effect on the MEA single fuel cell performance. MEA single-cell performance of oh-PtNi(Rh)/C_{KB} (blue), N-doped oh-PtNi(Rh)/C_{KB} (red), and Pt/C (black) as the cathode and Pt/C as the anode in H_2/O_2 (solid lines) and H_2/air (dashed lines). Polarization curves as a function of current density. The cathode loadings of oh-PtNi(Rh)/C_{KB} and N-doped oh-PtNi(Rh)/C_{KB} were 0.1 mg_{Pt} cm^{-2}, while the cathode loading for Pt/C was 0.2 mg_{Pt} cm^{-2}. The loading for the anode was 0.1 mg_{Pt} cm^{-2}. 100 RH% cell. Other test details are shown in the figure.

50 cm^2 MEA Fuel Cell Tests of oh-PtNi(Rh)/N-C. Fig. 6 displays the very first 50 cm^2 single PEM fuel cell polarization curves employing shape-selective octahedral cathode catalysts. The cell tests were carried out in pure oxygen (for catalyst activity) and in H_2/Air stoic 2/2 conditions (for cell performance) using the "aa" treated oh-PtNi(Rh)/C, oh-PtNi(Rh)/N-C samples and a reference 50 wt% Pt/C catalyst. It is important to note that the cathode loading of the reference 50 wt% Pt/C was 0.2 mg_{Pt} cm^{-2}, twice that of the shaped octahedral nanoparticles of 0.1 mg_{Pt} cm^{-2}. We note that the Pt/C reference is measured at twice the loading in comparison to the other catalysts. This, in addition to the higher ECSA, affects positively the high current density performance. For comparison to a Pt/C catalyst at the same loading and similar ECSA, we refer to reference,[29] where an annealed 30 Pt wt% Pt/C was reported to have mass activity at 0.9 V and ECSA of 0.15 A mg_{Pt}^{-1} and 45 m^2 g_{Pt}^{-1}, respectively. The experimental PEMFC performance are given in Table 2. The morphologies of the "aa" post synthesis treated oh-PtNi(Rh)/C, oh-PtNi(Rh)/N-C after the MEA test (Fig. S25) revealed some agglomeration of nanoparticles with few particles preserving their shape (as shown in green circles).

Table 2. Effect of N doping in MA and high current density performance in MEA-based Fuel cell of annealed/acid washed "aa" samples with loading of 0.1 mg_{Pt} cm^{-2} and Pt/C2 sample with double loading of 0.2 mg_{Pt} cm^{-2}

Catalyst	*ECSA Wet ($m^2 g_{Pt}^{-1}$)*	*Mass activity @ 0.9 V ($A\ mg_{Pt}^{-1}$)*	*Specific activity @ 0.9 V ($\mu A\ cm^{-2}$)*	*High current density @ 0.6 V ($mA\ cm^{-2}_{geo}$)*
aa-PtNi(Rh)/C_{KB}	30.3	0.35	1031	1531
aa-PtNi(Rh)/N-C_{KB}	35.0	0.35	995	1488
Pt/C2	55.3	0.27	604	> 2000

As shown in Table 2, the N-doped carbon supported oh-PtNi(Rh) catalysts revealed slightly higher ECSA values than the undoped one (the CO stripping plots are shown in Fig. S24). The shaped oh-PtNi(Rh) catalysts exhibited an unprecedented, exceptionally high current density of ~ 1500 mA cm^{-2}. Their MA were essentially identical, while the high current densities at 0.6 V exhibited showed a difference of 50 mA cm^{-2}. While the ORR Pt mass activity of the PtNi(Rh) turned out inferior to oh-PtNi(Mo)/C_V, the value of 0.35 A mg_{Pt}^{-1} at 0.9 V_{cell} clearly exceeded reference Pt/C.[6, 29]

Based on previous work,[18, 33] N-doped carbon improves the ionomer distribution in the catalyst layer, that may improve proton and oxygen mass transport. Nonetheless, this enhancement was not apparent under the current conditions. Plausible reason for this is either that Ni ion leaching suppressed the proton transport enhancement effect, due to Ni ion poisoning effects; or that, since the polarization curves shown in Figure 6 were measured under full humidity, the enhancement for the proton transport and oxygen mass transport showed little difference under this condition. Therefore, a supporting measurement was performed at lower relative humidity, 30 RH%. The MEA measurement results of aa oh-PtNi(Rh)/C, aa oh-PtNi(Rh)/N-C samples under 30 RH% showed no significant difference, either, (Fig. S26), thus supporting the hypothesis of the leached Ni cations ionomer interaction.

To seek more experimental evidence to support our hypothesis, pure 50 wt% Pt nanoparticle reference cathode catalysts were prepared on undoped and nitrogen-doped Ketjen Black EC-300J, with which catalyst inks, layers and MEAs were prepared as described in the experimental section with geometric Pt loadings of 0.2 mg Pt/cm^2. Fig. 7 displays the polarization curves of the 50 cm^2 single cells in H_2/O_2 and H_2/air at 80 °C recorded at 100% (Fig. 7a) and 30% (Fig. 7b) relative humidity at both anode and cathode.

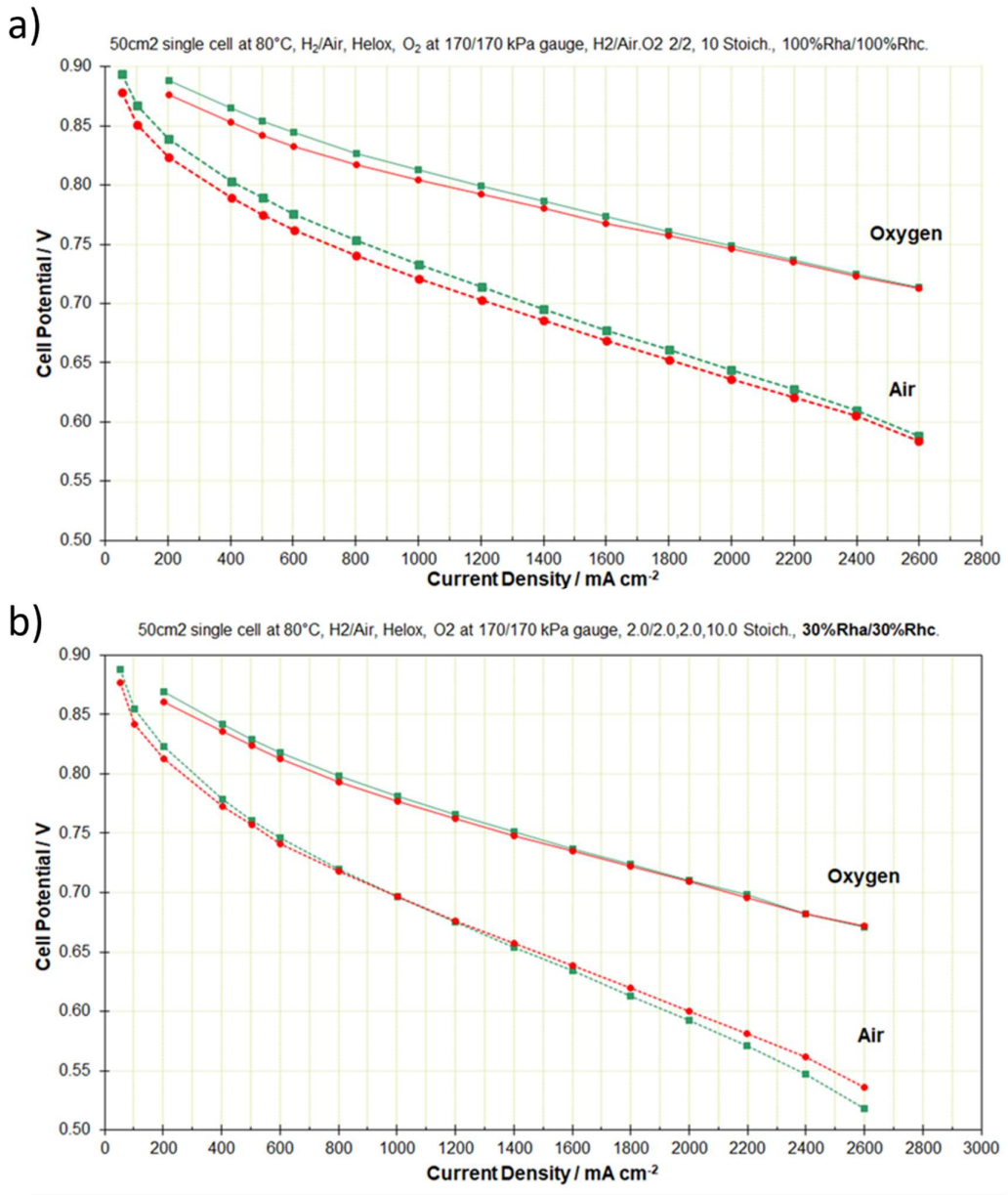

Figure 7. Effect of N-doping of cathode catalyst carbon supports on MEA single-cell performance. PEM fuel cells tested in H_2/air employed 50% Pt/C_{KB} (green) and 50% Pt/N-C_{KB} (red) electrocatalyst layers at the cathode and Pt/C electrocatalyst layers at the anode. Polarization curves as a function of current density. The cathode loadings were 0.2 mg_{Pt} cm^{-2}. The loading for the anode was 0.1 mg_{Pt} cm^{-2}. Relative cell humidity was (a) 100% RH and (b) 30% RH. Other test details are given in the figure.

50% Pt/N-C_{KB} (red in Fig. 7a) showed a loss of kinetic activity relative to the un-doped 50% Pt/C_{KB} (green), but its performance increased with current density, and approaches a crossover point at the highest current densities. In contrast, under the drier conditions (Fig. 7b) the performance of 50% Pt/N-C_{KB} displays a significantly more beneficial mass transport

(less voltage losses at high current densities) above a current density of around 1 A/cm^2. This indicates improved water management at low RH in the MEA using the more hydrophilic N-doped carbon, likely thanks to a more homogeneous distribution of ionomer over the carbon surface. This is facilitated by the ionic interactions between the protonated nitrogen doped sites on carbon and the sulfonate groups of the ionomer.[32, 33] The 50% Pt/N-C_{KB} behavior lends much credibility to our conclusion that for catalyst layers with N-doped and un-doped oh-PtNi(Rh)/C_{KB}, electrostatic interactions between carbon and ionomer are hampered by leached Ni ions. In Table S16 the higher membrane resistance values of PtNi(Rh) catalysts may be caused by the Ni leaching phenomenon.

3. Conclusion

We have explored a combination of three distinct catalyst materials design strategies to improve the single PEM fuel cell performance of Rh-doped, N-doped carbon supported, octahedrally shaped oh-PtNiRh nanoparticle ORR catalysts deployed in catalyst layers of MEAs. Lack of translation of high catalytic ORR Pt mass activity observed in liquid RDE cells into relevant layer architectures of single PEM fuel cells has prompted this significant endeavor.

First, the chemical state and chemical-mechanistic role of catalyst surface Rh-dopant was examined by HR-TEM and operando X-ray absorption spectroscopy. It was shown that Rh atoms were randomly distributed on the nanoparticle surface and that Rh exists in the oh-PtNi(Rh) in the form of metal oxide clusters. Moreover, using *operando* XAS analysis, we have unraveled how the oxidation state of the Rh dopant changed with varying applied electrode potential, which further supports its presence as a surface dopant. Electrochemical measurements confirmed reduced kinetic activity losses of Rh-doped oh-PtNi(Rh) catalyst over Mo-doped ones, leading to enhanced stability. This was also consistent with the good morphological stability of the octahedral shape after the stability test.

The second strategy aimed at fabricating higher Pt wt% layers with high catalytic activity. Thus, a series of Rh-doped PtNi octahedral nanocatalysts with different loading on different carbons was successful synthesized, and the catalysts were down selected in terms of ORR activities in RDE measurements. The most promising catalysts consisted in ~30 Pt wt% on Ketjen Black carbon.

The third strategy consisted in N doping of carbon supports in order to induce ionomer-support interactions to lower proton and oxygen transport losses at high powers.

Combining all three strategies, we demonstrated the first 50 cm^2 single PEM cell performance of the resulting Rh-doped shape-controlled oh-PtNi(Rh), supported on N-doped Ketjen Black. The catalysts featured an ORR Pt mass activity at 0.9 V of 0.35 A mg_{Pt}^{-1} and displayed a previously unachieved high current density of 1488 mA cm^{-2} at 0.6 V. Leaching and dispersion of Ni cations from the alloy catalyst into the ionomer, affecting the ionomer interaction, is concluded to be responsible for muted impact of N-doping strategies in combination with alloy catalysts. This conclusion is supported by the significantly improved MEA performance

observed with N-doped carbon supported pure Pt nanoparticle catalysts where Ni leaching is absent.

In summary, a high Pt wt% loaded Rh-doped PtNi octahedral catalyst was synthesized and a new SoA high current density in MEA-based single cell for a shaped PtNi alloy was achieved. Based on our study, high Pt wt% loadings on carbon combined with high stability is recommended to PEM fuel cell practitioners for improving the actual cell performance of shaped PtNi octahedra. Suppressing Ni leaching remains a future challenge. Future studies should further improve the chemical and electrochemical stability of the metal nanoparticles to fully translate their performance from RDE to MEA.

Acknowledgement

The collaborative GAIA EU research and development project has received funding from the Fuel Cells and Hydrogen 2 Joint Undertaking under grant agreement No 826097. This Joint Undertaking receives support from the European Union's Horizon 2020 - Research and Innovation Framework Programme, Hydrogen Europe and Hydrogen Europe Research. The authors are grateful for the financial support by the Deutsche Forschungsgemeinschaft (DFG) under the grant number HE 7192/1-2. We acknowledge the support of Hitachi High-Technologies. We thank the Zentraleinrichtung Elektronenmikroskopie (ZELMI) of Technische Universität Berlin for their support with TEM measurements. We thank Johnson Matthey Hydrogen Technologies Ltd. (UK) for supporting with the commercial catalyst. We also acknowledge Pohang Light Source II and the beam-scientist for the support. We thank Jessica Hübner, Dr. Elisabeth Hornberger and Dr. Hong Nhan Nong, (Technische Universität Berlin), for contributing to data collection at the synchrotron radiation sources. We thank the beam scientists Dr. Martin Radtke and Kirill Zusenko as well as the beamline BAMline of BESSY II, Berlin, respectively.

References

1. Huang, X.; Zhao, Z.; Cao, L.; Chen, Y.; Zhu, E.; Lin, Z.; Li, M.; Yan, A.; Zettl, A.; Wang, Y. M.; Duan, X.; Mueller, T.; Huang, Y., ELECTROCHEMISTRY. High-performance transition metal-doped Pt(3)Ni octahedra for oxygen reduction reaction. *Science* **2015,** *348* (6240), 1230-4.
2. Bu, L.; Guo, S.; Zhang, X.; Shen, X.; Su, D.; Lu, G.; Zhu, X.; Yao, J.; Guo, J.; Huang, X., Surface engineering of hierarchical platinum-cobalt nanowires for efficient electrocatalysis. *Nat Commun* **2016,** *7*, 11850.
3. Beermann, V.; Gocyla, M.; Kuhl, S.; Padgett, E.; Schmies, H.; Goerlin, M.; Erini, N.; Shviro, M.; Heggen, M.; Dunin-Borkowski, R. E.; Muller, D. A.; Strasser, P., Tuning the Electrocatalytic Oxygen Reduction Reaction Activity and Stability of Shape-Controlled Pt-Ni Nanoparticles by Thermal

Annealing - Elucidating the Surface Atomic Structural and Compositional Changes. *J Am Chem Soc* **2017,** *139* (46), 16536-16547.
4. Wang, X. X.; Swihart, M. T.; Wu, G., Achievements, challenges and perspectives on cathode catalysts in proton exchange membrane fuel cells for transportation. *Nature Catalysis* **2019,** *2* (7), 578-589.
5. Osmieri, L.; Park, J.; Cullen, D. A.; Zelenay, P.; Myers, D. J.; Neyerlin, K. C., Status and challenges for the application of platinum group metal-free catalysts in proton-exchange membrane fuel cells. *Current Opinion in Electrochemistry* **2021,** *25*.
6. Sun, Y.; Polani, S.; Luo, F.; Ott, S.; Strasser, P.; Dionigi, F., Advancements in cathode catalyst and cathode layer design for proton exchange membrane fuel cells. *Nat Commun* **2021,** *12* (1), 5984.
7. Gasteiger, H. A.; Kocha, S. S.; Sompalli, B.; Wagner, F. T., Activity benchmarks and requirements for Pt, Pt-alloy, and non-Pt oxygen reduction catalysts for PEMFCs. *Appl Catal B-Environ* **2005,** *56* (1-2), 9-35.
8. Kang, Y.; Cretu, O.; Kikkawa, J.; Kimoto, K.; Nara, H.; Nugraha, A. S.; Kawamoto, H.; Eguchi, M.; Liao, T.; Sun, Z.; Asahi, T.; Yamauchi, Y., Mesoporous multimetallic nanospheres with exposed highly entropic alloy sites. *Nat Commun* **2023,** *14* (1), 4182.
9. Stamenkovic, V. R.; Fowler, B.; Mun, B. S.; Wang, G.; Ross, P. N.; Lucas, C. A.; Markovic, N. M., Improved oxygen reduction activity on Pt3Ni(111) via increased surface site availability. *Science* **2007,** *315* (5811), 493-7.
10. Huang, X.; Zhu, E.; Chen, Y.; Li, Y.; Chiu, C. Y.; Xu, Y.; Lin, Z.; Duan, X.; Huang, Y., A facile strategy to Pt3Ni nanocrystals with highly porous features as an enhanced oxygen reduction reaction catalyst. *Adv Mater* **2013,** *25* (21), 2974-9.
11. Hornberger, E.; Mastronardi, V.; Brescia, R.; Pompa, P. P.; Klingenhof, M.; Dionigi, F.; Moglianetti, M.; Strasser, P., Seed-Mediated Synthesis and Catalytic ORR Reactivity of Facet-Stable, Monodisperse Platinum Nano-Octahedra. *ACS Applied Energy Materials* **2021,** *4* (9), 9542-9552.
12. Aran-Ais, R. M.; Dionigi, F.; Merzdorf, T.; Gocyla, M.; Heggen, M.; Dunin-Borkowski, R. E.; Gliech, M.; Solla-Gullon, J.; Herrero, E.; Feliu, J. M.; Strasser, P., Elemental Anisotropic Growth and Atomic-Scale Structure of Shape-Controlled Octahedral Pt-Ni-Co Alloy Nanocatalysts. *Nano Lett* **2015,** *15* (11), 7473-80.
13. Chen, Q.; Cao, Z.; Du, G.; Kuang, Q.; Huang, J.; Xie, Z.; Zheng, L., Excavated octahedral Pt-Co alloy nanocrystals built with ultrathin nanosheets as superior multifunctional electrocatalysts for energy conversion applications. *Nano Energy* **2017,** *39*, 582-589.
14. Huang, X.; Zhao, Z.; Cao, L.; Chen, Y.; Zhu, E.; Lin, Z.; Li, M.; Yan, A.; Zettl, A.; Wang, Y. M.; Duan, X.; Mueller, T.; Huang, Y., High-performance transition metal–doped Pt3Ni octahedra for oxygen reduction reaction. *Science* **2015,** *348* (6240), 1230-4.
15. Choi, S. I.; Xie, S.; Shao, M.; Odell, J. H.; Lu, N.; Peng, H. C.; Protsailo, L.; Guerrero, S.; Park, J.; Xia, X.; Wang, J.; Kim, M. J.; Xia, Y., Synthesis and characterization of 9 nm Pt-Ni octahedra with a record high activity of 3.3 A/mg(Pt) for the oxygen reduction reaction. *Nano Lett* **2013,** *13* (7), 3420-5.
16. Zhao, Z.; Feng, M.; Zhou, J.; Liu, Z.; Li, M.; Fan, Z.; Tsen, O.; Miao, J.; Duan, X.; Huang, Y., Composition tunable ternary Pt-Ni-Co octahedra for optimized oxygen reduction activity. *Chem Commun (Camb)* **2016,** *52* (75), 11215-11218.
17. Zhang, C.; Sandorf, W.; Peng, Z., Octahedral Pt2CuNi Uniform Alloy Nanoparticle Catalyst with High Activity and Promising Stability for Oxygen Reduction Reaction. *ACS Catalysis* **2015,** *5* (4), 2296-2300.
18. Lim, J.; Shin, H.; Kim, M.; Lee, H.; Lee, K. S.; Kwon, Y.; Song, D.; Oh, S.; Kim, H.; Cho, E., Ga-Doped Pt-Ni Octahedral Nanoparticles as a Highly Active and Durable Electrocatalyst for Oxygen Reduction Reaction. *Nano Lett* **2018,** *18* (4), 2450-2458.
19. Beermann, V.; Gocyla, M.; Willinger, E.; Rudi, S.; Heggen, M.; Dunin-Borkowski, R. E.; Willinger, M. G.; Strasser, P., Rh-Doped Pt-Ni Octahedral Nanoparticles: Understanding the

Correlation between Elemental Distribution, Oxygen Reduction Reaction, and Shape Stability. *Nano Lett* **2016,** *16* (3), 1719-25.
20. Urchaga, P.; Kadyk, T.; Rinaldo, S. G.; Pistono, A. O.; Hu, J.; Lee, W.; Richards, C.; Eikerling, M. H.; Rice, C. A., Catalyst Degradation in Fuel Cell Electrodes: Accelerated Stress Tests and Model-based Analysis. *Electrochimica Acta* **2015,** *176*, 1500-1510.
21. Riese, A.; Banham, D.; Ye, S.; Sun, X., Accelerated Stress Testing by Rotating Disk Electrode for Carbon Corrosion in Fuel Cell Catalyst Supports. *Journal of The Electrochemical Society* **2015,** *162* (7), F783-F788.
22. Polymeros, G.; Baldizzone, C.; Geiger, S.; Grote, J. P.; Knossalla, J.; Mezzavilla, S.; Keeley, G. P.; Cherevko, S.; Zeradjanin, A. R.; Schüth, F.; Mayrhofer, K. J. J., High temperature stability study of carbon supported high surface area catalysts—Expanding the boundaries of ex-situ diagnostics. *Electrochimica Acta* **2016,** *211*, 744-753.
23. Schmidt, T. J.; Gasteiger, H. A.; Stäb, G. D.; Urban, P. M.; Kolb, D. M.; Behm, R. J., Characterization of High‐Surface‐Area Electrocatalysts Using a Rotating Disk Electrode Configuration. *Journal of The Electrochemical Society* **2019,** *145* (7), 2354-2358.
24. Higuchi, E.; Uchida, H.; Watanabe, M., Effect of loading level in platinum-dispersed carbon black electrocatalysts on oxygen reduction activity evaluated by rotating disk electrode. *Journal of Electroanalytical Chemistry* **2005,** *583* (1), 69-76.
25. Kelly, M. J.; Fafilek, G.; Besenhard, J. O.; Kronberger, H.; Nauer, G. E., Contaminant absorption and conductivity in polymer electrolyte membranes. *Journal of Power Sources* **2005,** *145* (2), 249-252.
26. Kienitz, B.; Pivovar, B.; Zawodzinski, T.; Garzon, F. H., Cationic Contamination Effects on Polymer Electrolyte Membrane Fuel Cell Performance. *Journal of The Electrochemical Society* **2011,** *158* (9).
27. Durst, J.; Chatenet, M.; Maillard, F., Impact of metal cations on the electrocatalytic properties of Pt/C nanoparticles at multiple phase interfaces. *Phys Chem Chem Phys* **2012,** *14* (37), 13000-9.
28. Braaten, J. P.; Xu, X.; Cai, Y.; Kongkanand, A.; Litster, S., Contaminant Cation Effect on Oxygen Transport through the Ionomers of Polymer Electrolyte Membrane Fuel Cells. *Journal of The Electrochemical Society* **2019,** *166* (16), F1337-F1343.
29. Dionigi, F.; Weber, C. C.; Primbs, M.; Gocyla, M.; Bonastre, A. M.; Spori, C.; Schmies, H.; Hornberger, E.; Kuhl, S.; Drnec, J.; Heggen, M.; Sharman, J.; Dunin-Borkowski, R. E.; Strasser, P., Controlling Near-Surface Ni Composition in Octahedral PtNi(Mo) Nanoparticles by Mo Doping for a Highly Active Oxygen Reduction Reaction Catalyst. *Nano Lett* **2019,** *19* (10), 6876-6885.
30. Li, S., Numerical Investigation on the Impact of Membrane Thickness on Transport Phenomena in PEM Fuel Cells. *International Journal of Electrochemical Science* **2020**, 4138-4147.
31. Parnière, A.; Blanchard, P.-Y.; Cavaliere, S.; Donzel, N.; Prelot, B.; Rozière, J.; Jones, D. J., Nitrogen Plasma Modified Carbons for PEMFC with Increased Interaction with Catalyst and Ionomer. *Journal of The Electrochemical Society* **2022,** *169* (4).
32. Orfanidi, A.; Madkikar, P.; El-Sayed, H. A.; Harzer, G. S.; Kratky, T.; Gasteiger, H. A., The Key to High Performance Low Pt Loaded Electrodes. *Journal of The Electrochemical Society* **2017,** *164* (4), F418-F426.
33. Ott, S.; Orfanidi, A.; Schmies, H.; Anke, B.; Nong, H. N.; Hubner, J.; Gernert, U.; Gliech, M.; Lerch, M.; Strasser, P., Ionomer distribution control in porous carbon-supported catalyst layers for high-power and low Pt-loaded proton exchange membrane fuel cells. *Nat Mater* **2020,** *19* (1), 77-85.
34. Gan, L.; Cui, C.; Heggen, M.; Dionigi, F.; Rudi, S.; Strasser, P., Element-specific anisotropic growth of shaped platinum alloy nanocrystals. *Science* **2014,** *346*, 1502-1506.
35. Jia, Q.; Zhao, Z.; Cao, L.; Li, J.; Ghoshal, S.; Davies, V.; Stavitski, E.; Attenkofer, K.; Liu, Z.; Li, M.; Duan, X.; Mukerjee, S.; Mueller, T.; Huang, Y., Roles of Mo Surface Dopants in Enhancing the ORR Performance of Octahedral PtNi Nanoparticles. *Nano Lett* **2018,** *18* (2), 798-804.

36. Cui, C.; Gan, L.; Heggen, M.; Rudi, S.; Strasser, P., Compositional segregation in shaped Pt alloy nanoparticles and their structural behaviour during electrocatalysis. *Nat Mater* **2013,** *12* (8), 765-71.
37. Imhof, T.; Della Bella, R. K. F.; Stuhmeier, B. M.; Gasteiger, H. A.; Ledendecker, M., Towards a realistic prediction of catalyst durability from liquid half-cell tests. *Phys Chem Chem Phys* **2023**.

Supporting Information

Enhancing the Performance of Shape-controlled Octahedral Rhodium Doped PtNi Nanoalloys inside Hydrogen-air Fuel Cell Cathodes Using a Rational Design of Catalysts, Supports and Layering

L. Pan,[1] A. Parnière,[2] O. Dunseath,[3] D. Fongalland,[3] G. Nicolau,[3] C. C. Weber,[1] J. Lu,[1] M. Klingenhof,[1] A. Arinchtein,[1] H.-S. Oh,[4] P.-Y. Blanchard,[2] S. Cavaliere,[2,5] M. Heggen,[6] R. E. Dunin-Borkowski,[6] A. Martinez Bonastre,[3] F. Dionigi,[1] J. Sharman,[3] D. Jones[2] and P. Strasser[1]**

[1] Technische Universität Berlin, Straße des 17. Juni 124 – 10623, Berlin – Germany.

[2] ICGM, Univ. Montpellier, CNRS, ENSCM, 34095 Montpellier cedex 5, France.

[3] Johnson Matthey Technology Centre, Blount's Court, Sonning Common, Reading RG4 9NH, United Kingdom

[4]Clean Energy Research Center, Korea Institute of Science and Technology, 02792, Seoul, Republic of Korea.

[5] Institut Universitaire de France (IUF), 1 rue Descartes, 75231 Paris cedex 05, France.

[6] Ernst Ruska-Centre for Microscopy and Spectroscopy with Electrons, Forschungszentrum Jülich GmbH, 52425 Jülich, Germany.

*Corresponding author

pstrasser@tu-berlin.de

fabio.dionigi@tu-berlin.de

Experimental Section

- Chemicals and materials

Platinum (II) acetylacetonate [$Pt(acac)_2$] (Pt 48.0% min) and nickel (II) acetylacetonate [$Ni(acac)_2$] (95%) were purchased from Alfa Aesar. Rhodium acetylacetonate (97%), benzoic acid (BA, ≥99.5%), N,N-dimethylformamide (DMF, 99.8%) were purchased from Sigma-Aldrich. Carbon Vulcan (XC72R) was purchased from Cabot. Ketjen Black EC-300 J was purchased from Nouryon. For the washing, ethanol (VWR, absolute, ≥99.8%), acetone (Sigma-Aldrich, ≥99.5%) and ultrapure water (Milli-Q, 18.2 MΩ) were used. All the chemicals were used as received without further purification.

- Catalyst synthesis
  - PtNiRh on carbon in small batches (~ 100 mg)

The Rh-doped PtNi/C catalyst was obtained by the further growth of Rh on the preformed octahedral PtNi/C catalyst. The synthesis of 20 Pt wt% V19 is similar and adapted from.[1, 2] 48 mg of $Pt(acac)_2$ (122 µmol), 24 mg of $Ni(acac)_2$ (93.4 µmol) and 360 mg BA were added into an autoclave glass cylinder. Meanwhile 80 mg of the carbon (Vulcan carbon) was dispersed in 40 mL DMF by a horn sonifer (Branson Sonifier® SLPe) for 15 min. The carbon suspension was poured carefully into the glass liner and went for 15 min ultrasonic bath treatment. Later, the glassware was sealed in the autoclave (Roth High-pressure autoclave Model I). During the solvothermal reaction, the mixture was heated up to 160 °C for 12 h with continuous stirring. The autoclave was cooled down to RT and opened. In the second step, additional precursors, $Pt(acac)_2$ (12.0 mg, 30.5 µmol), $Ni(acac)_2$ (6.0 mg, 23.3 µmol) and $Rh(acac)_3$ (10.8 mg, 27 µmol) were dissolved in 10 mL DMF under ultrasonic condition and added into the glass liner. The liner was put in the sonic bath for 30 min for mixing and then transferred back into the autoclave for the next period of reaction. It was heated to 170 °C and held for 48 h with stirring. Subsequently, the cleaning procedure was carried out. The sample was washed 4 times with respectively ethanol/acetone, ethanol/acetone, ethanol/pure water, pure water. To separate out the product, the solution with washing solvents was centrifugated and the solid precipitated. After washing procedure, the sample was freeze-dried in the vacuum dryer overnight.

The composition of the as prepared catalyst V19 was $Pt_{64.9}Ni_{33.1}Rh_{2.0}$ and the platinum weight loading are 19.31 wt%. For XAs experiments a replica was prepared showing extremely good reproducibility, with composition of $Pt_{65.9}Ni_{32.8}Rh_{1.3}$ and a platinum weight loading of 23.8 wt%.

The catalyst supported on Ketjen Black EC-300J was synthesized with the same procedure but with different carbon source. Its composition was $Pt_{68.7}Ni_{30.9}Rh_{0.4}$ and platinum loading as much as 20 wt%.

The steps for the synthesis of the higher platinum weight loading (30 Pt wt%) catalysts were similar, but the amount of the precursors and BA were increased with a factor of 2 achieving the 2 times of platinum weight loading, while the DMF and carbon amount remained the

same. The as prepared catalyst on carbon Vulcan had a composition as $Pt_{64.5}Ni_{31.9}Rh_{3.6}$ with eventually 34.6 Pt wt% and the one on Ketjen Black EC-300J has outcome with 30.5 Pt wt% with $Pt_{63.0}Ni_{32.6}Rh_{4.4}$.

- Unsupported PtNiRh nanoparticles synthesis and impregnation on the supports

48 mg of $Pt(acac)_2$ (122 µmol), 24 mg of $Ni(acac)_2$ (93.4 µmol) and 360 mg BA were added with 40 mL DMF into an autoclave glass cylinder. The precursor suspension was sonifered in a bath sonifer for 15 min. The cylinder was put into the autoclave and well-sealed. During the solvothermal reaction, the mixture was heated up to 160 °C for 12 h with continuous stirring. When the heating was finished, the autoclave was cooled down to RT and opened. Afterwards, additional precursors, $Pt(acac)_2$ (12.0 mg, 30.5 µmol), $Ni(acac)_2$ (6.0 mg, 23.3 µmol) and $Rh(acac)_3$ (10.8 mg, 27 µmol) were dissolved in 10 mL DMF under ultrasonic condition and added into the glass liner. The glass was put in the sonic bath for 30 min for mixing and then transferred back into the autoclave for the next period of reaction. It was heated to 170 °C and held for 48 h with stirring and afterwards cooled down to RT. The suspension was separated into two portions, they were impregnated and supported onto 0% N-doped Ketjen Black carbon (as purchased) and 3% N-doped Ketjen Black carbon (with N-doping pre-treatment) respectively. Thereafter, the same washing and drying procedure as the supported PtNi(Rh) catalysts were accomplished. This assured that the NPs in both batches were intrinsically identical. The batch supported on 0.5% N-doped carbon was reproduced with the same process.

- Scale-up catalyst synthesis (~ 1 g scale)

Scale-up of octahedral (oh-) shape-controlled nanoparticles. 480 mg carbon source (undoped without N-functionality and doped with N-functionality) was weighed into two centrifuge tubes with in total 90 mL DMF, and the carbon suspension was horn-sonificated for 15 min in an ice-water bath. After strong ultrasonication, the carbon suspension was transferred into an autoclave glass cylinder, another 100 mL DMF was added and mixed in the autoclave without heating for the overnight mixing. Precursor solution was prepared, $Pt(acac)_2$ (432.0 mg, 1098.4 µmol, 1.31 equiv. relative to $Ni(acac)_2$), $Ni(acac)_2$ (216 mg, 840.8 µmol, 1.00 equiv.) and benzoic acid (3240 mg, 26.5 mmol) and were added into a centrifuge tube with 50 mL DMF for 10 min in a sonification bath. The precursor solution was then added dropwise with pipette into the carbon suspension in the reactor vessel, which was finally sonicated in the bath sonification for 40 minutes. After this step the glass cylinder was put into an autoclave (Parr Instrument, Seires 4568) for another 2 hours stirring under 45 °C for better distribution of reactants. The autoclave was heated to 160 °C for 12 hours with stirring in the meantime of the solvothermal treatment. The autoclave was cooled down to room temperature and opened.

For the surface doping of the PtNi/C-nanoparticles, the suspension mentioned above was taken out of the autoclave and set aside. $Pt(acac)_2$ (108mg, 274.6 µmol), $Ni(acac)_2$ (54 mg, 210.2 µmol) and $Rh(acac)_3$ (64.8mg, 162 µmol) was dissolved in 60 mL DMF. Afterwards this precursor solution was dropwise added into the reactor glass liner containing the undoped suspension with a pipette under sonification (in a sonification bath) for 40 minutes. Same as the first step, after transferring into the autoclave, the solution was stirred in the autoclave for 2 hours under 50 °C. Then it was heated up until 170 °C for 48 hours. The autoclave was cooled down to the room temperature and a washing process was conducted. The sample was washed 4 times with respectively ethanol/acetone, ethanol/acetone, ethanol/pure water, pure water. To separate out the product, the solution with washing solvents was centrifugated and the solid precipitated. After washing procedure, the sample was frozen and dried in the vacuum dryer overnight.

- Post-treatment for the catalyst

Post-treatment consists of firstly an annealing process and secondly a leaching process.

  - Annealing

The catalyst was ground and placed as homogenously as possible in a ceramic oven crucible with a cover. This cover was placed to avoid mass loss due to the gas flow since the powder was light and the upmost part could fly away in the oven. Then crucible was placed in the middle of the oven to be heated evenly, and nitrogen was flowed through with the same flow rate as later hydrogen gas for 30 min to remove all the oxygen in the chamber. Then the gas was changed to hydrogen, flowing for 30 min. With a heating ramping of 5 K/min, the catalyst was heated up to 350 °C for 2 h. After the heating procedure, the catalyst was cooled down naturally until *ca.* 50-60 °C and then the gas flow was changed to nitrogen until the chamber was cooled down to RT.

  - Acid-leaching

The catalyst powder was immersed in an acid solution of 0.1 M $HClO_4$, identical as the electrolyte in RDE measurement, for 12 h. Then the upper solution part was poured out carefully without wasting much catalyst, the catalyst was washed with DI water for 3 times, and finally freeze dried overnight.

- Preparation of the N-doped KB carbon

KB carbons were treated by nitrogen plasma using an Europlasma instrument including a 13.56 MHz RF generator and a primary pump (Edwards). 400 mg of Ketjen Black EC-300J carbon sample were dispersed in Petri dish of 18 cm diameter and pre-treated at 90 °C overnight in a vacuum desiccator (Vacuo Temp) at 280 mbar. The Petri dish containing the sample was then placed in the plasma chamber and the carbon submitted to plasma treatment for 2 hours at 300 W under nitrogen atmosphere with a nitrogen gas flow of 100

sccm (Air Liquide Alphagaz 2 99.9999 %), leading to carbon samples with 2.9 – 3.1 % nitrogen, as determined by elemental analysis.

- XRD

X-ray diffraction patterns were collected on a Bruker D8 Advance (Siemens KFL Cu 2K X-ray tube and Lynx Eye Detektor) diffractometer in Bragg Brentano geometry using a Cu Kα1. The patterns were recorded between 20-90° with a step size of 0.04°.

- ICP-OES

An inductively coupled plasma optical emission spectroscopy (ICP-OES) analysis was used to determine the elemental composition of the synthesized particles using a 715-ES-ICP analysis system (Varian). The selected wavelengths for the concentration determination were 203.604; 212.863; 214.424; 217.468; 265.945; 306.471 nm for Pt. For Ni they were 216.555; 221.648; 222.486; 227.021; 230.078; 230.299 nm. For Rh were 343.488; 369.236 nm.

- TEM

Transmission electron microscopy (TEM) images were recorded on a FEI Tecnai G2 20 S-TWIN with a LaB6 cathode operating with 200 kV acceleration voltage and a resolution limit of 0.24 nm. Samples were dispersed in isopropanol and drop casted on a Cu grid (400 mesh).

- STEM

High-resolution STEM was conducted on a Cs-probe corrected Hitachi HF5000 microscope operating at 200 kV. Compositional maps were obtained by energy-dispersive X-ray spectroscopy (EDS) using double EDX Ultra 100 detectors from Oxford Instruments.

- Ex situ and Operando XAS

In situ X-ray absorption spectroscopy (XAS) at the Rh K-edge of PtNiRh catalyst was performed at the BAMline of Bessy II operated by the Helmholtz-Zentrum Berlin für Materialien und Energie GmbH. X-ray absorption spectra were recorded in the fluorescence mode using a scintillation detector. The samples (composition: $Pt_{65.9}Ni_{32.8}Rh_{1.3}$, and 23.81 Ptwt% on Vulcan carbon XC72R) were deposited by drop casting from an ink on carbon paper stripes that were previously cut from a gas diffusion layer (GDL) sheet (28BC, SIGRACET®, SGL group). After drying in an oven, the edge of the GDL stripe far from the sample was wrapped with copper tape and electrically contacted by a crocodile clip in order to be used as the working electrode. A Pt wire was used as counter electrode and an Ag/AgCl electrode, previously calibrated versus a reversible hydrogen electrode, as reference electrode. The electrolyte was 0.1 M $HClO_4$, and was injected with a pipette in a home-made PEEK cell which had two openings covered by PEEK foil as X-Ray windows. The cell was placed at 45° in respect to the incident beam and the detector. The sample loading was 80 times the loading used in RDE, so ~0.8 mg_{Pt} cm^{-2}. Reference metal foils were measured in transmission at the same time for energy alignment. The sample was measured

in the dry state, then the electrolyte was inserted and the same protocol that was used in RDE measurements was applied (PEIS, 50 CV, 3 CV, PEIS) for the catalyst activation. Then a series of CA potential steps was conducted: 0.05 V_{RHE}, 0.78 V_{RHE}, 1.00 V_{RHE}. After 20 minutes of potential hold at each potential step, XAS was measured. Initial processing of the XAS data was performed using the program Athena. [3] The spectra were smoothed by boxcar, kernel size 9 (see Supp Fig S8).

Pt L_3-edge, Ni K-edge and Rh K-edge were measured ex situ at the Pohang Light Source (PLS) synchrotron, Pt edge at the 1D KIST-PAL beamline and Rh and Ni edges at the HF-XAFS B/L beamline. Initial processing of the XAS data was performed using the program Athena and the program Artemis was used for fitting the extended X-ray absorption fine structure (EXAFS).[3] For the reference foils, fits were done in *R*-space, $k^{1,2,3}$ weighting. 1.35< R < 3.2 Å and Δk = 3.00 – 12.00 $Å^{-1}$ for Pt L3-edge data, 1.30 < R < 2.80 Å and Δk = 3.0 – 13.8 $Å^{-1}$ for the Ni K-edge data, and 1.0 < R < 3.1 Å and Δk = 3.00 – 14.00 $Å^{-1}$ for the Rh K edge. The fitting results of the E_0 at the Pt L3, Ni K and Rh K edges are 9.4 ± 0.5 eV, 6.0 ± 0.4 eV and -5.0 ± 0.6, respectively. R-factor: 0.0023 for Pt, 0.0010 for Ni and 0.0049 for Rh. N was set to 12 for Pt, Ni and Rh and all have fcc structure. For the PtNiRh sample, Ni and Pt edges were co-fit. Basic constraint introduced: $\sigma^2_{Pt\text{-}Ni} = \sigma^2_{Ni\text{-}Pt}$. S_0^2 was fixed at 0.74, 0.86 and 0.58 for Pt, Ni and Rh, respectively as obtained by fitting the reference foils. Fits were done in *R*-space, $k^{1,2,3}$ weighting. 1.23< R < 3.35 Å and Δk = 3.00 – 12.00 $Å^{-1}$ were used for fitting the Pt L3-edge data, 1.0 < R < 3.0 Å and Δk = 3.0 – 12.0 $Å^{-1}$ for the Ni K-edge data, and 0.82< R < 2.14 Å and Δk = 3.00 – 12.00 $Å^{-1}$ for the Rh edge. The fitting results of the E_0 at the Pt L_3, Ni K and Rh K edges are 8.1 ± 1.8 eV, 4.3 ± 1.1 eV and 2.1 ± 1.2, respectively. R-factor: 0.0093 for the co-fit of Ni and Pt, and 0.0090 for Rh.

- XPS

The nitrogen speciation of the N-doped carbon was determined by X-ray photoelectron spectroscopy (XPS) using an ESCALAB 250 spectroscope from Thermo Electron with an Al K_α ray (1486.6 eV) as monochromatic excitation source. A surface area of 500 µm of diameter was analysed. The emitted photoelectrons were detected perpendicularly to the sample surface with a constant analyser energy mode (20 eV pass energy). Deconvolution of the spectra was carried out using the Avantage software with mixed Lorentzian-Gaussian contributions. Binding energies (BEs) of all core levels are referenced to the C=C contribution of C 1 s spectrum at 284.4 eV.

- RDE
  - Ink preparation

To prepare an ink 2.5 mg of catalyst with 20 Pt wt% were added into 1.99 mL water, 5 µL Nafion (5 wt%) and 0.5 mL isopropanol (≥ 99.5 %) and horn ultrasonicated (Branson Sonifier 150) for 30 minutes. For the catalysts with 30 Pt wt%, around 1.7 mg powder was added into the identical ink solvent recipe and dispersed the same way. 10 µL of the ink were placed on a glassy carbon (GC) rotating disk electrode (diameter Ø=5 mm), which results in a Pt loading of 10 µg cm^{-2}. The film was dried at 50 °C for 10 minutes.

- Electrochemical characterization

For electrochemical characterizations, a conventional three electrode cell with a Pt mesh as counter electrode (Pt furled mesh Pt 5x5 cm^2), a reference electrode (MMS Hg/Hg_2SO_4 with the calibrated potential E= -0.725 V_{RHE}) and a glassy carbon working electrode was used. The working electrode was always immersed into the electrolyte under potential control at 0.05 V_{RHE}. A 0.1 M $HClO_4$ was used for electrochemical measurements (diluted from 70 % conc. $HClO_4$, 99.999 % trace metal bases, Sigma Aldrich with milli-Q water). All measurements were performed with a BioLogic Science Instruments potentiostats SP-150 and SP-200. The degree of purity for the gases used was 99.998 % for oxygen, 99.999 % for nitrogen, and 99.999 % for hydrogen (used for the reference electrode calibration).

- Activation step and H_{upd}-ECSA evaluation

GC working electrode potential was lowered at 0.05 V_{RHE} while rotating at 1600 rpm and the rotation was stopped when in position without bubbles on the electrode surface.

The electrochemical activation was performed *via* potential cycling between 0.05 and 0.925 V_{RHE} with a scan rate of 100 mV s^{-1} for 50 times under nitrogen atmosphere. the next 3 cycles were applied within the same potential range at 20 mV s^{-1}. The third cycle of the 20 mV s^{-1} scan was used to determine the electrochemical catalytic surface are (ECSA) from hydrogen under potential deposition (H_{upd}).

H_{upd}-ECSA Evaluation: the current of the cyclic voltammogram (CV) was background subtracted. The values were calculated integrating in cathodic sweeping between around 0.05 and 0.4 V. The integration range was between the cathodic currents corresponding to the capacitive background current and the current before the hydrogen evolution reaction onset (HER). The measured Q_H value was normalized with respect to the theoretical value of Q_H^{theo} = 210 µC cm^{-2}, which is assuming a one electron transfer between one H atom and one Pt atom, forming a hydrogen monolayer and normalized by the scan rate.

- Catalytic activity for oxygen reduction reaction

The catalytic activity of the catalysts was measured by linear sweep voltammetry. The measurement of the background current was conducted in a potential range between 0.05 and 1.0 V_{RHE} with a scan rate of 20 mV s^{-1} and a rotation speed of 1600 rpm in nitrogen saturated electrolyte (at least 15 min bubbling). The scan was repeated once. Then the working electrode was elevated above the liquid and oxygen was bubbling through the electrolyte for at least 15 min. Then the test was performed in oxygen saturated electrolyte in the same potential range with a scan rate of 20 mV s^{-1} for 3 times and a scan rate of 5 mV s^{-1} once under a rotation speed of 1600 rpm. The kinetic currents were calculated using the Koutecky-Levich equation,

$$1/j = 1/jk + 1/jd$$

where j was measured at 0.9 V_{RHE} and j_d was determined in the diffusion limited current area and j_k is the calculated kinetic current density. Both currents obtained from the test were IR corrected firstly, where the resistance R was determined by potential electrochemical impedance spectroscopy at 0.5 V_{RHE}, and then subtracted with the background current, which was the current from the cathodic voltammetry sweeping in N_2 saturated electrolyte at 0.4 V_{RHE}. The mass activity was calculated based on the kinetic current normalized by Pt weight loading and corresponding specific activity was normalized by the H_{upd}-ECSA.

- Stability test

The stability test was conducted after the electrochemical activation, impedance spectrometry and activity measurement. Stability measurements have been performed via potential cycling between 0.6 and 0.925 V_{RHE} with a scan rate of 100 mV s^{-1} and in N_2 saturated electrolyte for 10k cycles without working electrode rotating. In the meanwhile, the N_2 was flown above the electrolyte level. After the stability test protocol, CV was applied to obtain the H_{upd}-ECSA in the catalyst state "after the stability test": 3 times at 100 mV s^{-1} and 3 times at 20 mV s^{-1}. Then, impedance spectroscopy and the ORR test procedure were also implemented.

- CO stripping

CO stripping experiments were performed following ORR activity test. For a sample tested with the stability protocol test, the CO stripping was performed following the ORR activity test after the stability test, not the ORR activity test before the stability test. This is due to the fact that the surface composition may alter after the CO stripping, due to the interaction of surface Pt or Ni atoms with CO. Thus, the CO stripping is the last electrochemical test step in the RDE.

For CO stripping, 0.05 V_{RHE} was applied and the rotation was set to 400 rpm after bubbling N_2 for minimum 15 min. Then CO was bubbled for another 5 min at the same rotation speed. The gas was switched back to N_2 and the electrolyte was bubbled for another 10 min to remove CO in the electrolyte. Then the rotation was turned off after the removal of bubbles on the electrode surface. Then 3 cyclic voltammetry cycles were recorded at 20 mV s^{-1} between 0.05 V_{RHE} and 1 V_{RHE}, while venting N_2 above the electrolyte. The oxidation of surface adsorbed CO (assumed as one mono layer) occurred during the first scanning CV, the corresponding oxidation was represented by the CO stripping peak. The IR corrected current of the first positive scan was deducted by one of the second positive scan, which was considered as the background current. Then the integral of the peak in the range where the current was positive was calculated and translated based on an assumption of one layer of CO, which occupied a charge of 420 µC cm^{-2}.

- 80 °C RDE stability test

The tests were performed up to 10 000 cycles using on “aa” oh-PtNiRh catalyst. The configuration of the experimental cell was consisted of a jacket RDE cell, with water circulating into and out of the jacket to keep the electrolyte as warm as 80 °C. The working electrode preparation and ink recipe was same as room temperature RDE to stay consistent. Electrolyte used was $HClO_4$ 0.1 M. Reference electrode was a RHE electrode. A condenser was combined to an opening to avoid the severe evaporation overnight (around 18 h). Other openings were covered by PARAFILM® or plugs. The AST protocol was the same as adopted before in this study.

- MEA fabrication (JM)

The membrane electrode assemblies (MEAs) used in this work consist of five layers. Nafion 1100EW (equivalent weight in g polymer/mol H^+) was used to fabricate thin-layer electrodes. The cathode catalyst layers were prepared at an ionomer/carbon weight ratio of ca. 0.8/1 ~ 0.9/1 and metal loadings of ca 0.10 and 0.20 mg_{Pt} cm^{-2}. The anode catalyst layer was kept constant at an ionomer/carbon weight ratio of ca. 1.5/1 and a metal loading of 0.1 mg_{Pt} cm^{-2}. The membrane used was a perfluorosulfonic acid type, fabricated at JMFC with a thickness of ca. 20 µm. Catalyst layers were produced on a PTFE substrate and transferred via a decal method onto the membrane. Single cells (50 cm^2 active area) were assembled by sandwiching the catalyst coated membranes between the GDLs and applying an average compression onto the active area.

- MEA operating conditions

The fuel cell station was built in-house at JMFC. Pure oxygen and synthetic air were used as cathode reactants and pure H_2 as the anode reactant (all gases of 99.9% purity). Stoichiometric flow rates of anode (s = 2) and cathode (s = 9.5 for O_2 and s = 2 for air) reactants were used at current densities >0.2 A cm^{-2} and constant flows (corresponding to 0.2A cm^{-2} flows) at <0.2 A cm^{-2}. Reactant humidification was achieved by water-bubblers, the temperatures of which were calibrated to yield the desired relative humidity (RH) values. Humidity and cell pressure were measured at the inlet for both electrodes. Cell resistances as a function of current density (i.e., the sum of the proton-conduction resistance in the membrane and the various electronic resistances, bulk and contact resistances) were determined using an AC perturbation of 1 kHz at three different current densities of 25, 50 and 100 mA cm^{-2} and also using a current interrupt method. For each data point, the cell voltage was stabilized for 4 min where the current was measured. Multiple-path serpentine flow-fields (two and three parallel channels for the anode and cathode, respectively) machined into sealed graphite blocks were used for testing.

The MEAs were conditioned by the application of a constant current density of 500 mA cm^{-2} under H_2/Air at 50 kPa gauge, 100% RH and 80 °C. The cell voltage was monitored until a stable value was observed. The conditioning step lasted 2h unless specified otherwise. Afterwards the cathode catalyst layer was exposed to a series of cathode starvation steps followed by 2h current hold at 500 mA cm^{-2} until a stable voltage was observed. The cathode starvation step (purging of cathode compartment with pure nitrogen) reduces the

cathode voltage to below 0.1 V and it is intended to provide an electrochemical cleaning step for the cathode catalyst before measuring its activity under H_2/O_2.[4] After the starvation steps the MEA was ready for testing by H_2/O_2 polarization curves for MA quantification (50 kPa gauge, 100% RH and 80 °C). The polarization curves were recorded from low (i.e., 0.05 A cm^{-2}) to high current (i.e., 2 A cm^{-2}) ascending direction and backwards, descending direction. The lower current density limit was determined by maintaining the stoichiometry, at even lower currents there would be a risk of working under over-stoichiometric conditions with the used setup. The current density was maintained for 3 minutes at each step and the MA value was obtained from the ascending polarization curve at 0.9 V by extrapolation, after correction for the cell ohmic resistance. For this study, H_2 crossover current densities were measured using the procedure described by Kocha et al.[5]. In this test the hydrogen that permeates through the membrane to the cathode is oxidized by the application of a voltage (typically 250-300 mV are sufficient, and the latest above 400 mV one is in the mass transport limit) and the resulting current measured. Therefore, the cell was operated under H_2/N_2 and the gas crossover measurements were done at each of the operating conditions (i.e., temperature and H_2-partial pressure). The catalyst mass activity was not corrected on the basis of H_2-crossover current densities, i_{eff} (i.e., $i_{eff} = i + i_x$). Under the conditions used in this work ix was on the order of 2–5 A cm^{-2}. Performance curves in 50 cm^2 single cells were done with a three-way switch polarization curve in H_2 / (O_2, Helox and Air) at 100 kPa gauge-inlet and 80 °C. The cell current density was held for 10 min at each point and the cell voltage was averaged on the last minute. Cell performance in H_2/Air is plotted in the descending direction, from low currents to high currents. The cell resistance was calculated from the intercept at high frequency and the values obtained were 60±2 mOhm cm at 100 kPa gauge-inlet and 80 °C. Performance in H_2/Air was not iR corrected.

The ECSA was measured with the CO stripping method using the cell in half cell mode where the anode electrode acts as a pseudo reference electrode. The cathode voltage was controlled at 0.125 V at 80 °C, 100% RH and 50 kPa gauge whilst purging with 1% CO in N_2 at 300 ml min^{-1} for 15 min. Afterwards the cathode was purged with N2 at the same flow rate for 2 h to ensure that CO is removed from the bubblers and the catalyst layer pores. The adsorbed CO is oxidized electrochemically by scanning the cathode voltage from 0.125 V to 0.85 V and back to 0.05 V, at 20 mV s^{-1} for three cycles. The area under the CO oxidation peak is integrated by subtracting the third scan from the first scan and using a 420 µC cm^{-2} constant for a CO monolayer on Pt.

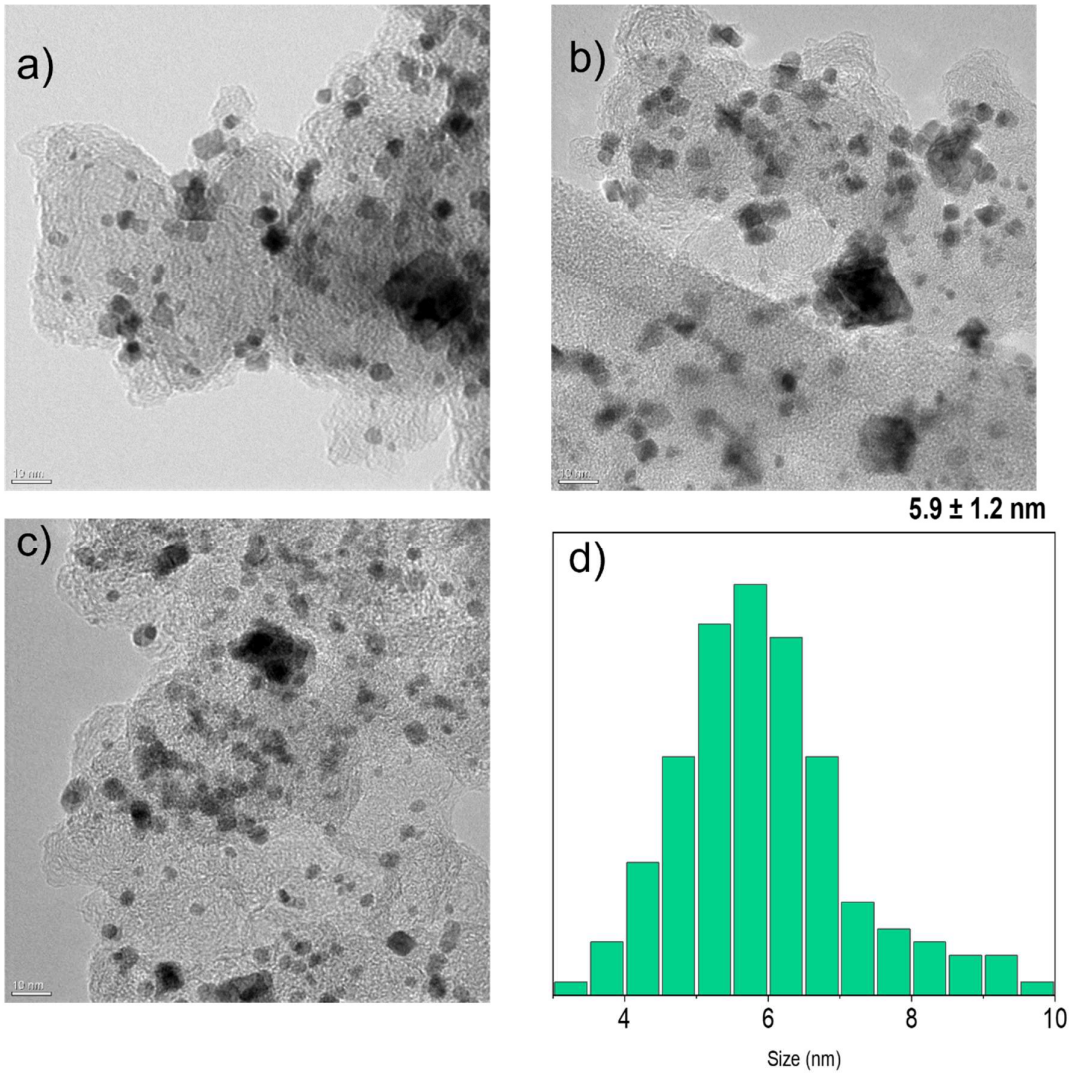

Fig. S1: TEM images of V-19 as prepared, after ink, after RDE stability. a) as prepared; b) after ink; c) after RDE stability; d) histogram of the particle size.

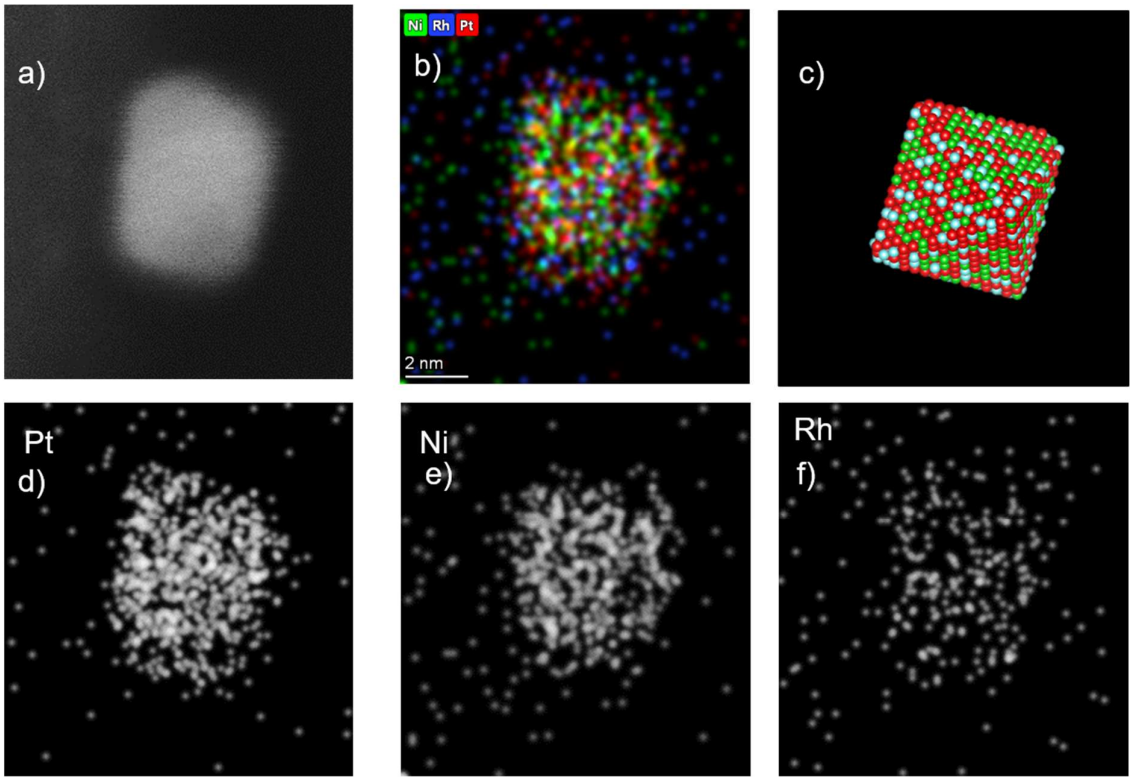

Fig. S2: HAADF and EDS of a single octahedron of V-19. EDX quantification: $Pt_{56.6}Ni_{38.8}Rh_{4.6}$

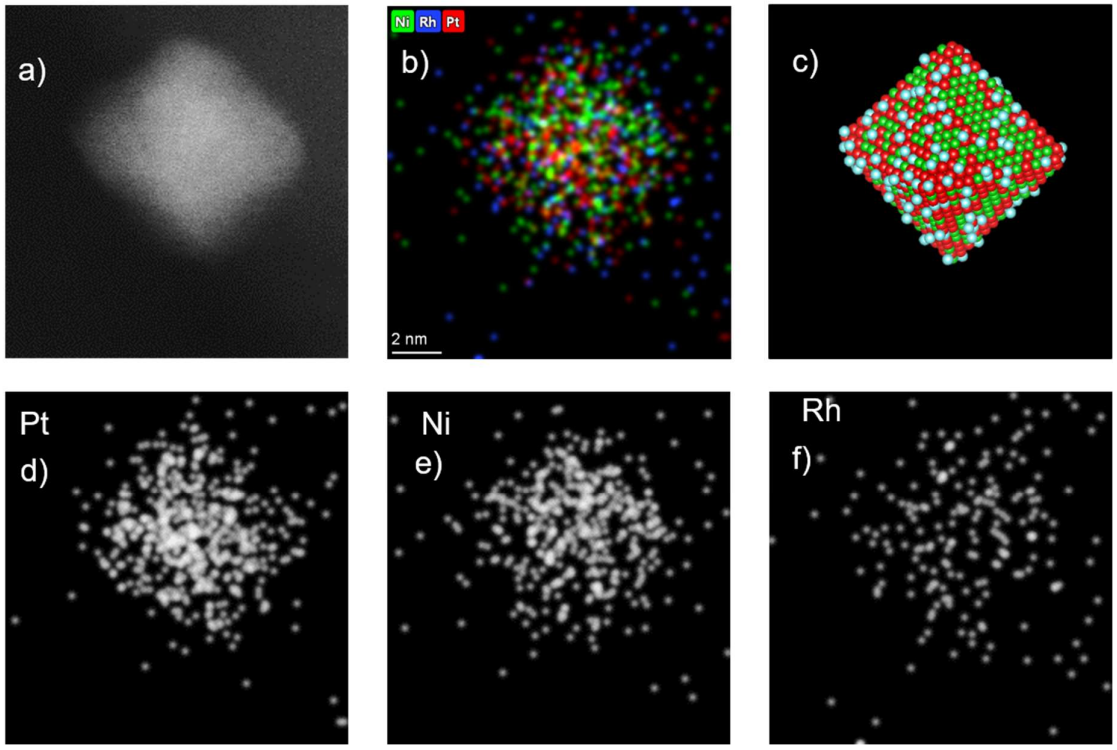

Fig. S3: HAADF and EDS of another example of single octahedron of V-19. EDX quantification: $Pt_{52.2}Ni_{42.9}Rh_{4.9}$

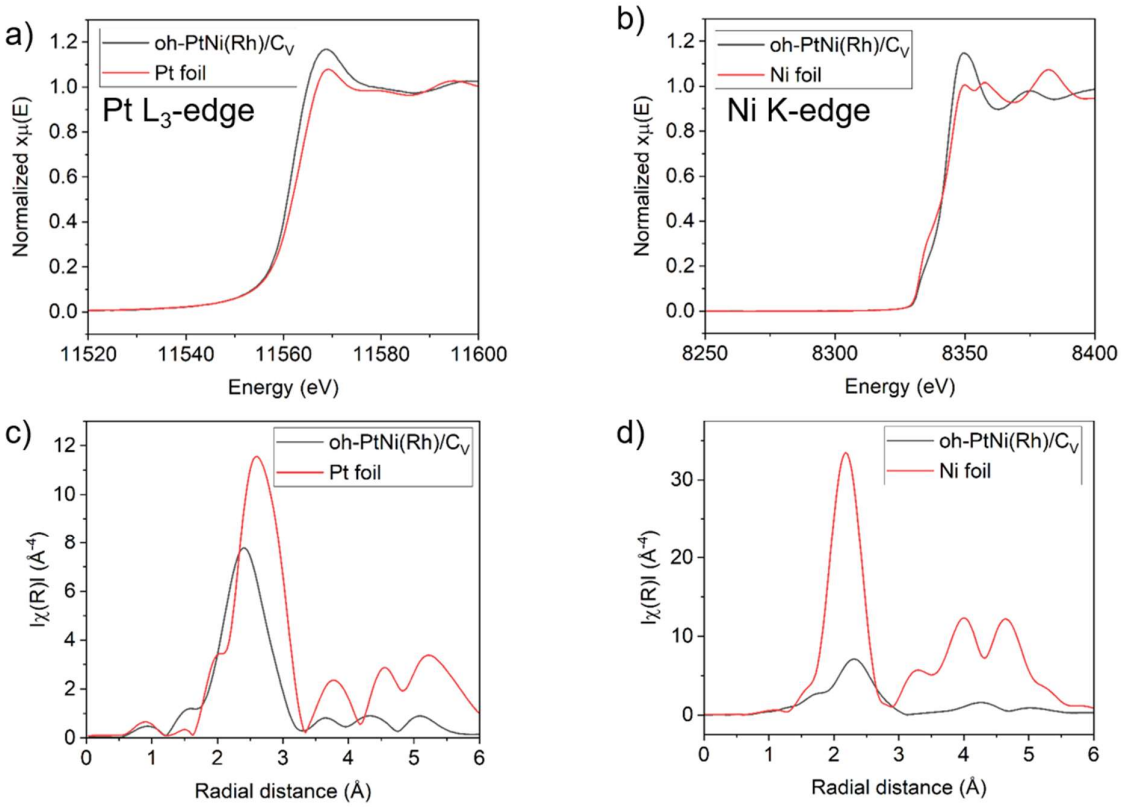

Fig. S4: XAS: Pt and Ni edge of oh-PtNi(Rh).

As supplementary for Rh edge in XAS, we have also investigated the Pt and Ni edge of the sample. From the white line of two samples in Fig. S4, we can see that the intensity and peak shape, illustrating that the Pt in oh-PtNi(Rh) sample has higher oxidation state than the Pt foil, the Pt is in metallic form. In order to determine the data from extended X-ray absorption spectroscopy fine structure, the experimental data was converted to Fourier transform (FT) form. In Fig. S4c, the spectrum can be used for determine the bond distance, the interatomic distance is slightly shorter than the bulk Pt, showing a contraction effect, possibly due to the PtNi alloy formation. The XAS spectrum for Ni K-edge was presented in Fig. S4b and it is shown that in the spectrum, the position of the edge was not overlapping with the Ni foil and shifted from the it, moreover, the intensity and peak was higher than the Ni foil, so we can conclude that the Ni in the sample was mostly metallic. It is clear that in the EXAFS in Fig. S4d, the spectra at 2.3 Å in comparison with Ni foil was shifted towards higher degree, this could be due to the PtNi alloy.

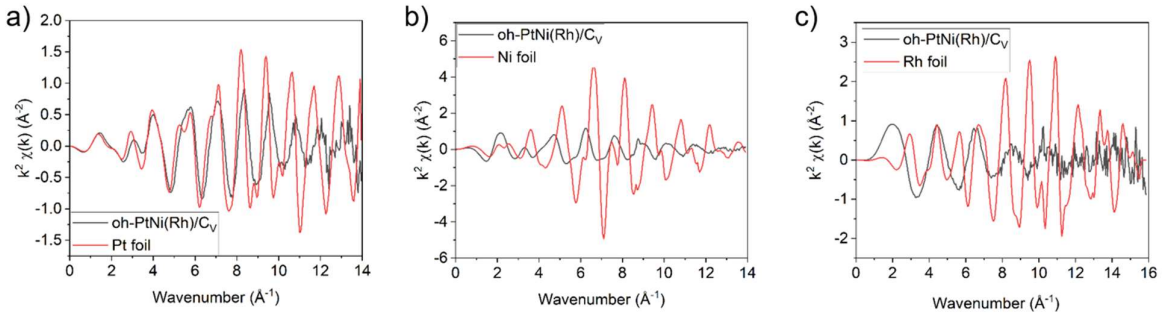

Fig. S5: K Space of XAS for a) Pt L-edge EXAFS, b) Ni K-edge and c) Rh L edge.

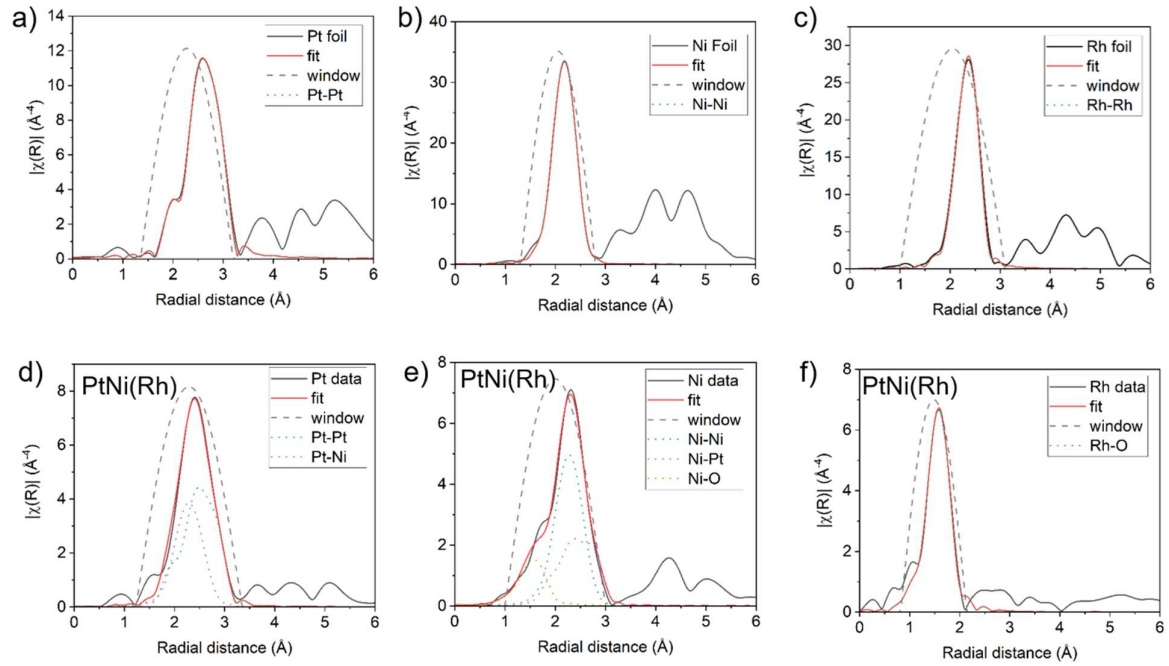

Fig. S6: EXAFS Fitting.

In accordance with the Fig. 2 and Fig. S4, the Pt in the oh-PtNi(Rh) can be fitted with Pt-Pt bonds and Pt-Ni bonds, it is clear that the shift of the Pt spectra shifted due to Pt-Ni bonding formation. For Ni, besides, Ni-Ni, Ni-Pt also oxidized Ni were observed with the curve fitting. Also, the Ni-Ni bonding was stretched than in Ni foil. For Rh metal, mostly fitted with oxidized Rh, corresponding with the data in Fig.2.

Following are the tables for fitting.

Table S1: EXAFS fitting of reference Pt foil

	Pt Edge Ex situ Values
$R_{Pt\text{-}Pt}$	2.762 +/- 0.003
$\sigma^2_{Pt\text{-}Pt}$	0.0041 +/- 0.0003
S_0^2	0.74 +/- 0.04

Table S2: EXAFS fitting of reference Ni foil

	Ni Edge Ex situ Values
$R_{Ni\text{-}Ni}$	2.483 +/- 0.002
$\sigma^2_{Ni\text{-}Ni}$	0.0065 +/- 0.002
S_0^2	0.86 +/- 0.03

Table S3: EXAFS fitting of reference Pt foil

	Rh Edge Ex situ Values
$R_{Rh\text{-}Rh}$	2.687 +/- 0.003
$\sigma^2_{Rh\text{-}Rh}$	0.0033 +/- 0.0003
S_0^2	0.58 +/- 0.04

Fits were done in *R*-space, $k^{1,2,3}$ weighting. 1.35< *R* < 3.2 Å and Δ*k* = 3.00 – 12.00 $Å^{-1}$ for Pt L3-edge data, 1.30 < *R* < 2.80 Å and Δ*k* = 3.0 – 13.8 $Å^{-1}$ for the Ni K-edge data, and 1.0 < *R* < 3.1 Å and Δ*k* = 3.00 – 14.00 $Å^{-1}$ for the Rh K edge. The fitting results of the E_0 at the Pt L3, Ni K and Rh K edges are 9.4 ± 0.5 eV, 6.0 ± 0.4 eV and -5.0 ± 0.6, respectively. R-factor: 0.0023 for Pt, 0.0010 for Ni and 0.0049 for Rh. N was set to 12 for Pt, Ni and Rh and all have fcc structure.

Table S4: EXAFS fitting of Pt in oh-PtNi(Rh)

	Pt Edge Ex situ Values
R_{Pt-Pt}	2.71 +/- 0.02
N_{Pt-Pt}	6.9 +/- 2.7
σ^2_{Pt-Pt}	0.0068 +/- 0.0025
R_{Pt-Ni}	2.63 +/- 0.02
N_{Pt-Ni}	3.6 +/- 1.4
σ^2_{Pt-Ni}	0.0092 +/- 0.0028

Table S5: EXAFS fitting of Ni in oh-PtNi(Rh)

	Ni Edge Ex situ Values
R_{Ni-Ni}	2.60 +/- 0.01
N_{Ni-Ni}	3.5 +/- 0.8
σ^2_{Ni-Ni}	0.010 +/- 0.002
R_{Ni-Pt}	2.65 +/- 0.01
N_{Ni-Pt}	3.3 +/- 1.1
σ^2_{Ni-Pt}	σ^2_{Pt-Ni}
R_{Ni-O}	2.00 +/- 0.02
N_{Ni-O}	1.9 +/- 0.6
σ^2_{Ni-O}	0.012 +/- 0.005

Table S6: EXAFS fitting of Rh in oh-PtNi(Rh)

	Rh Edge Ex situ Values
R_{Rh-O}	2.04 +/- 0.01
N_{Rh-O}	6.5 +/- 0.6
σ^2_{Rh-O}	0.0027 +/- 0.0011

Ni and Pt edges were co-fit. Basic constraint introduced: $\sigma^2_{Pt-Ni} = \sigma^2_{Ni-Pt}$. S_0^2 was fixed at 0.74, 0.86 and 0.58 for Pt, Ni and Rh, respectively as obtained by fitting the reference foils. Fits were done in *R*-space, $k^{1,2,3}$ weighting. 1.23< *R* < 3.35 Å and Δk = 3.00 – 12.00 $Å^{-1}$ were used for fitting the Pt L3-edge data, 1.0 < *R* < 3.0 Å and Δk = 3.0 – 12.0 $Å^{-1}$ for the Ni K-edge data, and 0.82< *R* < 2.14 Å and Δk = 3.00 – 12.00 $Å^{-1}$ for the Rh edge. The fitting results of the E_0 at the Pt L3, Ni K and Rh edges are 8.1 ± 1.8 eV, 4.3 ± 1.1 eV and 2.1 ± 1.2, respectively. R-factor: 0.0093 for the co-fit of Ni and Pt, and 0.0090 for Rh.

Table S7. N-doped C_V

Sample	Plasma			Nitrogen content (wt%)	Oxygen content (wt%)	BET (m^2g^{-1})
	N_2 flow (sccm)	Power (W)	Activation time (min)			
AP-V00	Non modified	Non modified	Non modified	**0**	0.926	240
AP-V05	100	300	240	**3.10**	6.08	160
AP-V06	100	300	30	**0.46**	2.17	220

Carbon black used: Vulcan XC72r. The plasma treatment is realized with a radiofrequency source at 13.56 MHz. AP-V00 is a non-modified sample and is considered as the reference. The nitrogen and oxygen contents were determined by EA.

Table S8.: ICP-OES of oh-PtNi(Rh) on N-doped C_V

	Oh-PtNi(Rh)/N-doped C_V			
	Pt wt%	Pt at%	Ni at%	Rh at%
Target (V19: PtNi(Rh) grown on C_V)	19.3	64.9	33.1	2.0
C_V	19.5	67.6	31.2	1.2
0.5%N-doped C_V	19.8	69.4	29.7	0.9
3%N-doped C_V	20.3	67.4	31.4	1.2

To better compare the N-doping effect, a batch of unsupported octahedra were separated into two batches and add to 0 %- and 3 % N-doping carbons. These are carbon-after method. The rests were synthesized with carbon-in method. Adding carbon support after the synthesis of PtNi octahedra is interesting for comparison of the support effect since the same batch of Pt alloy nanopartciles can be loaded on several supports suppressing the risk of variation in the synthesis of Pt alloy nanoparticles. In KB Pt nanoparticles can grow in pores with diameter below 4 nm, however it is difficult to grow octahedra with that small size (typical 6 nm and

up). Therefore, the mass activity cabn decrease. Loading the Pt nanopartciles afterwards might overcome this situation.

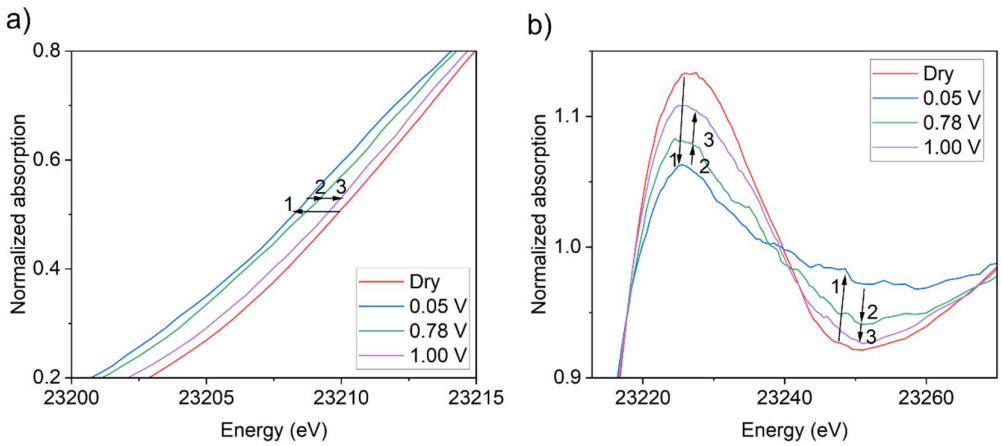

Fig. S7: Details of *operando* XANES Rh edge and white line of oh-PtNi(Rh).

More details about the Fig. 2e) are shown in Fig. S7. With respect to Rh energy edges, the energy edge of samples under 0.05 VRHE shifted towards lower energy than the dry sample and the white line intensity lower than the dry, indicating from as prepared sample to sample under applied potential of 0.05 V_{RHE}, there was a reduction reaction. With potential increasing, the oxidative state of Rh similarly increased due to the oxidation of Rh.

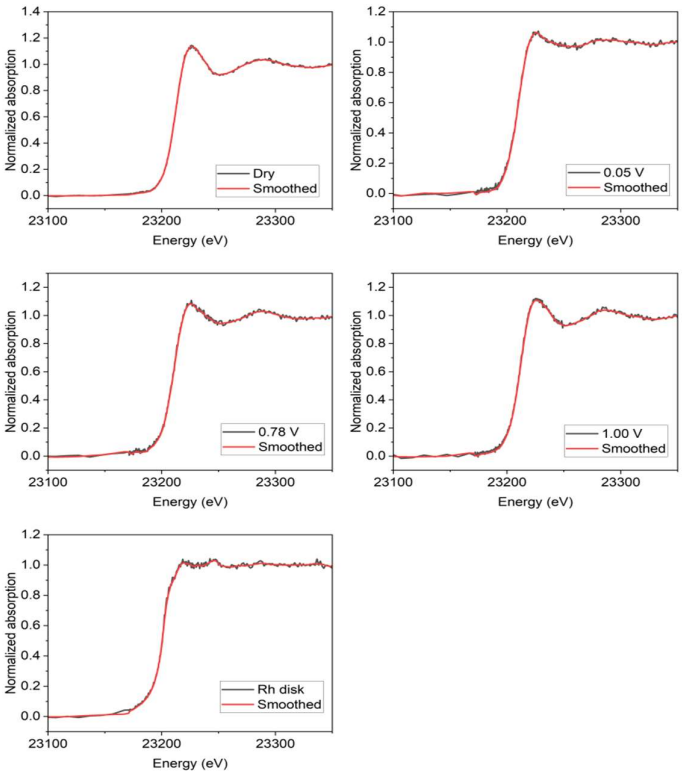

Figure S8: Curve smoothening of XANES Rh edge.

These curves were smoothed by boxcar, kernel size 9.

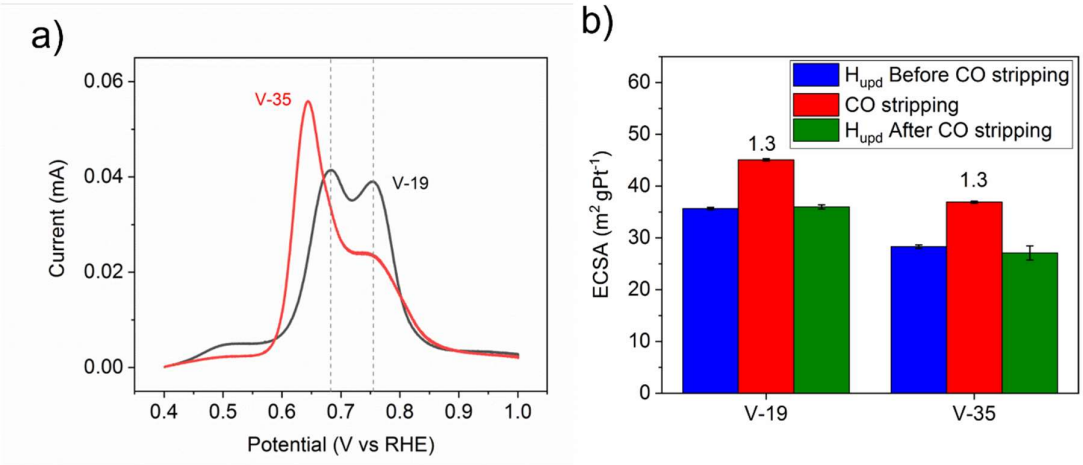

Fig. S9: CO stripping data of V-19 and V-35. a) CO stripping voltammogram of V-19 and V-35, curves were iR corrected and subtracted by the background currents. b) Comparison of H_{upd}-ECSA before and after the stability test and CO stripping for V-19 and V-35.

As seen in Fig. S9a), although the compositions shown in Table S1 of both samples were similar, the CO oxidation curves were different. Two CO stripping curves exhibited two peaks, however both peaks from V-35 compared with -19, shifted towards more negative potential. The difference in CO stripping could come from the agglomeration of nanoparticles,[6] or maybe despite of the analogous bulk composition, surface atomic arrangements not necessarily are the same. Considering the solid nature of carbon Vulcan and more severe agglomerate due to the higher loading, ECSAs of V-35 were generally smaller than V-19.

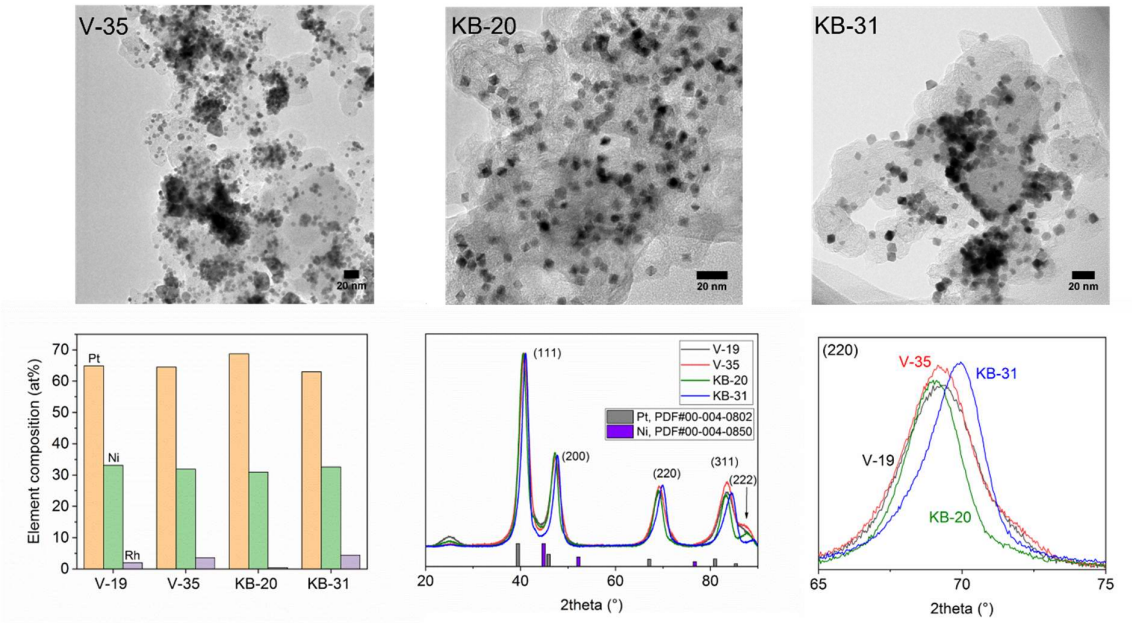

Fig. S10: Several physiochemical characterizations of sample. TEM images of sample V-35, KB-20 and KB-31. Elemental compositions based on ICP-OES. XRD patterns of oh-PtNi(Rh) catalysts on CV and CKB and at normal and high loading.

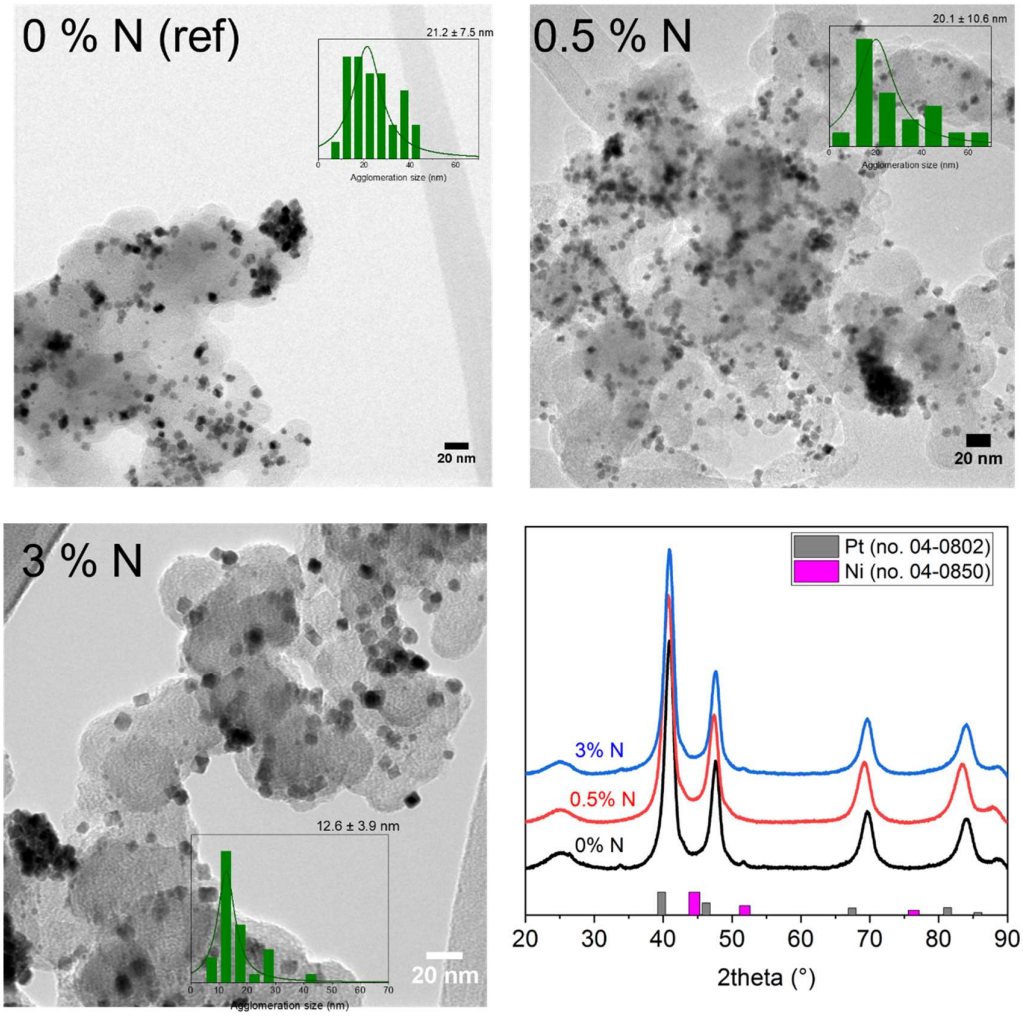

Fig. S11: TEM images with the histogram diagram of the agglomerations size distribution and XRD patterns of oh-PtNi(Rh) catalysts on support with different N amount.

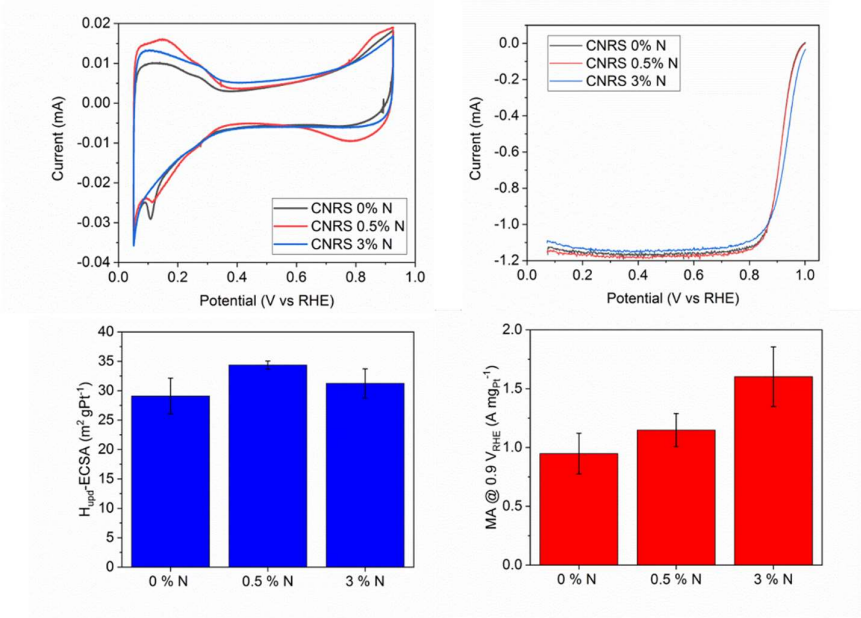

Figure S12: RDE data of samples supported on with different amount of N-doping.

In this study, for all the RDE measurements, the mass activities were taken and compared at 0.9 V_{RHE}, since the currents at 0.9 VRHE are reasonably apart from the diffusion limiting current, so in this case, we took the mass activity (MA) at 0.9 V_{RHE} to compare the electroactivity, instead of the choice of 0.95V_{RHE}, often additionally indicated for highly active catalysts.

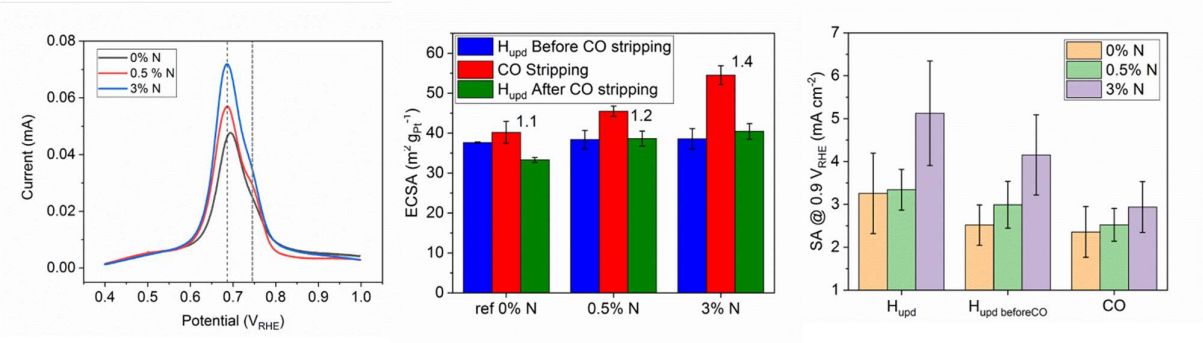

Figure S13: CO stripping data from RDE of samples supported on with different amount of N-doping.

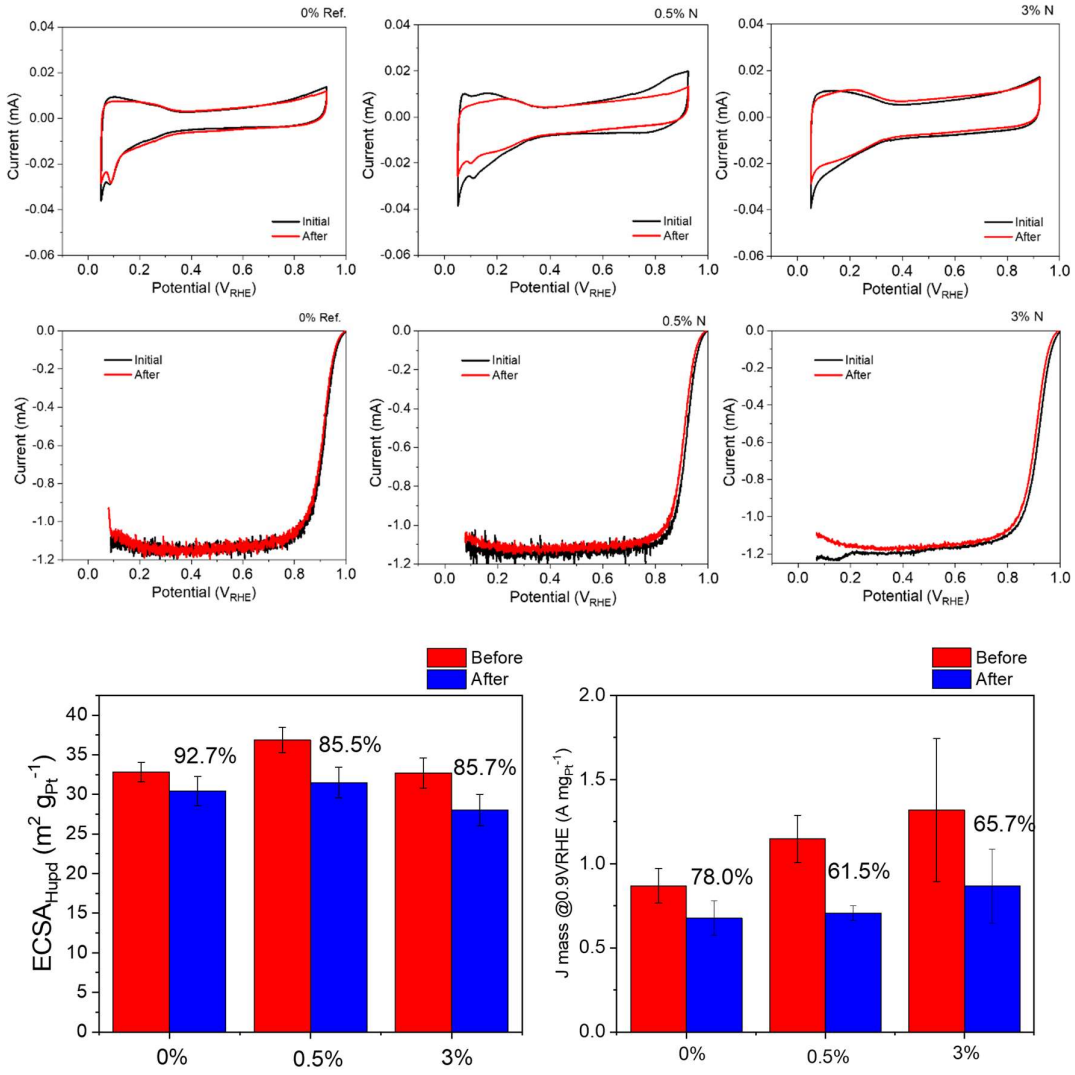

Figure S14. Stability test of oh-PtNi(Rh) on N-doped C_V with different amount of N-doping.

Table S9. Preparation details of N-doped KB carbons, elemental contents and BET surface areas.

Sample	Plasma			Nitrogen content (wt%)	Oxygen content (wt%)	BET (m^2g^{-1})
	N_2 flow (sccm)	Power (W)	Activation time (min)			
KB3-00 (C_{KB})	Non modified	Non modified	Non modified	**0.133 ± 0.004**	1.082 ± 0.226	800
KB3-32-3 (N-C_{KB})	100	300	120	**3.146 ± 0.336**	3.022 ± 0.449	780
KB3-32-4 (N-C_{KB})	100	300	120	**2.862 ± 0.167**	2.384 ± 0.298	780

Carbon source used was the KB EC300JD. KB3-32-3 and KB3-32-4 are two batches of the same carbon. KB3-00 is a non-modified sample and is considered as the reference. The nitrogen and oxygen contents were determined by EA.

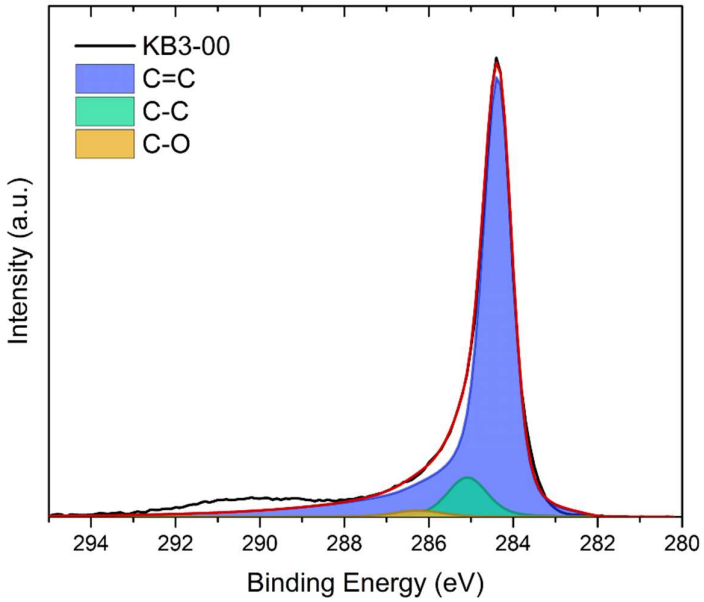

Fig S15. XPS data of KB3-00 (C_{KB}).

Table S10. XPS C peak fitting results of KB3-00 (C_{KB})

Contribution	Peak (eV)	at%
C=C	284.37	88.30
C-C	285.09	8.42
C-O	286.25	1.70

Table S11. XPS C peak fitting results of KB3-32 (C_{KB})

Contribution	Peak (eV)	At.%
C=C	284.41	65.66
C-C	285.20	11.43
C-O, C-N	286.01	6.05
C=O	287.16	4.12

Table S12. XPS N peak fitting results of KB3-32 (C_{KB})

Contribution	Peak (eV)	At.%
N pyridinic	398.26	2.60
N amine	399.19	2.82
N pyrrolic	400.15	2.34
N graphitic	401.15	0.94
N oxides	402.60	0.24

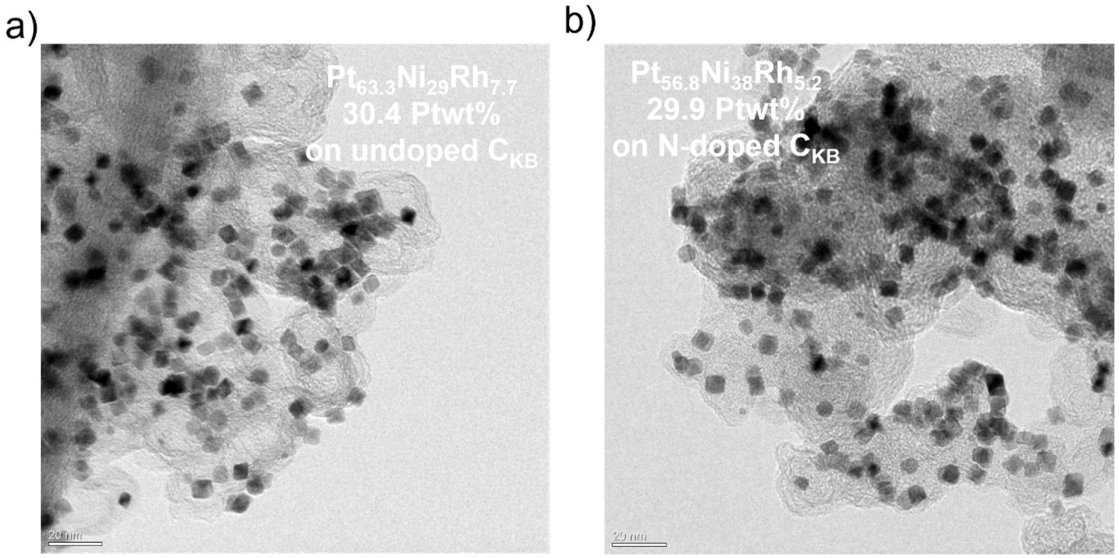

Fig. S16: TEM of upscaled 30 Pt wt% $Pt_2Ni_1(Rh)$ onto C_{KB} and N-doped $C_{KB.}$

The scale-up batches aimed at reproducing compositional $Pt_{63.0}Ni_{32.6}Rh_{4.4}/C_{KB}$ with 30 Pt wt% from a small batch synthesis. Both upscaled catalysts are done with the DMF-directed method. The yield of the synthesis was around 750 mg. From the TEM images, visible octahedras were formed in both samples. The compositions were similar and the ratio of Pt:Ni was around 2:1, while the sample on N-doped carbon showed slightly more Ni content than the other one.

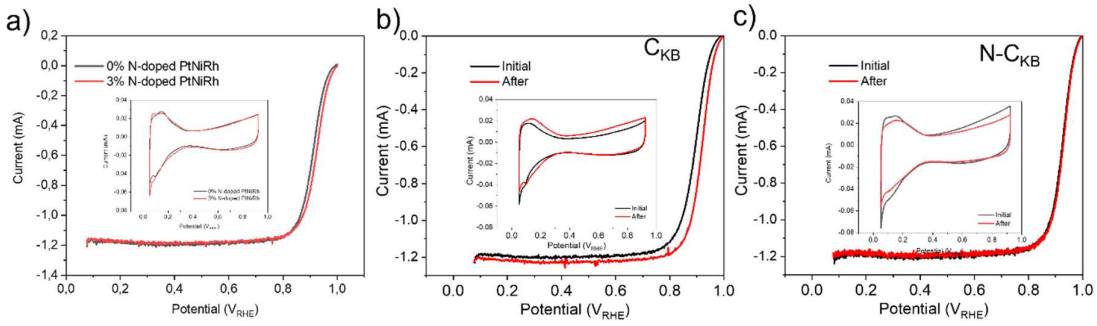

Fig. S17: CVs and LSVs for upscaled oh-PtNi(Rh) on C_{KB} and 3% N-doped $C_{KB.}$ a) comparison of CV and LSV for samples supported on C_{KB} and N-doped $C_{KB.}$ b) CVs and LSVs of Oh-PtNi(Rh) on C_{KB} before and after the stability test. c) CVs and LSVs of oh-PtNi(Rh) on N-C_{KB} before and after the stability test.

Table S13: MA and ECSAs from RDE measurements of scaled-up oh-PtNi(Rh) on C_{KB} and N-doped C_{KB} without any post-synthesis treatment.

	$ECSA_{Hupd}$ ($m^2 g_{Pt}^{-1}$)	MA@0.9 V_{RHE} (A mg_{Pt}^{-1})	$ECSA_{CO}$ ($m^2 g_{Pt}^{-1}$)
Small Scale (Target)	33.9 ± 1.4	0.94 ± 0.04	--
Upscaled on C_{KB}	35.3 ± 4.3 (after AST: 36.0 ± 5.2)	0.67 ± 0.17 (after AST: 0.91 ± 0.40)	49.0 ± 4.7
Upscaled on N-C_{KB}	42.3 ± 1.2 (after AST: 39.0 ± 2.2)	1.42 ± 0.22 (after AST: 1.91 ± 0.64)	53.0 ± 3.2 (after AST: 50.3 ± 2.4)

Both scaled-up catalyst batches shared a consistent result as the small batch. In view of H_{upd}-ECSA, both upscaled have large ECSAs, this could originate from the higher Ni content. Another interesting result was the stability in terms of MA was improved after the stability test for both large batches, this reverify the enhancement of stability in these Rh-doped samples.

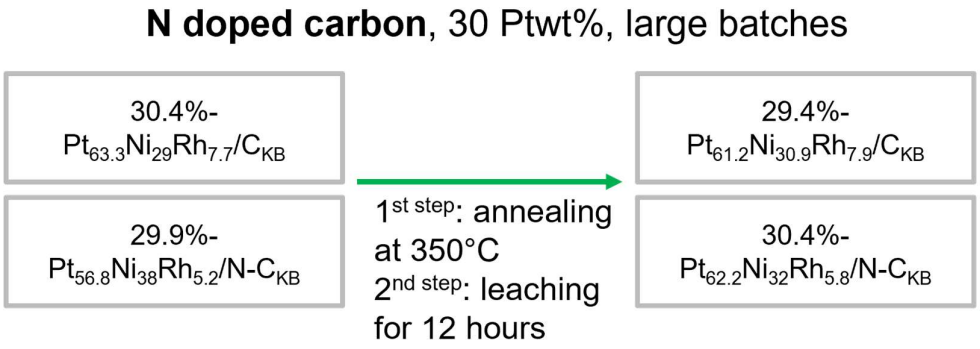

Fig S18: Schematic illustration of annealing/acid leaching "aa" post-treatments for scaled-up oh-PtNi(Rh) on C_{KB} and N-doped C_{KB}. The compositional information included.

After the treatment, 2 at% of Pt decreased, while Ni slightly increased in CKB. The origins of this difference are at the moment unclear, since Ni is not expected to increase. In contrast, 6 at% of Ni in N-C_{KB} was decreased. Due to this, after annealing/leaching process the Ni content

difference among the two samples is reduced after treatment, and now the samples have very close composition.

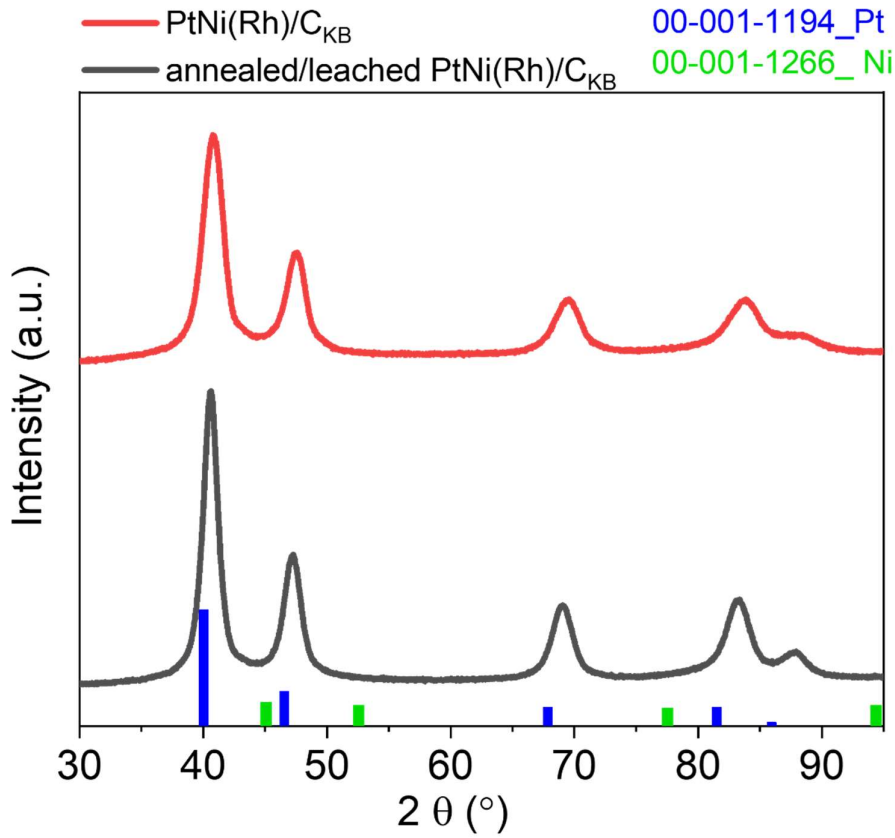

Fig, S19: XRD patterns of oh-PtNi(Rh)/C_{KB} catalysts before and after acid leaching and thermal annealing process.

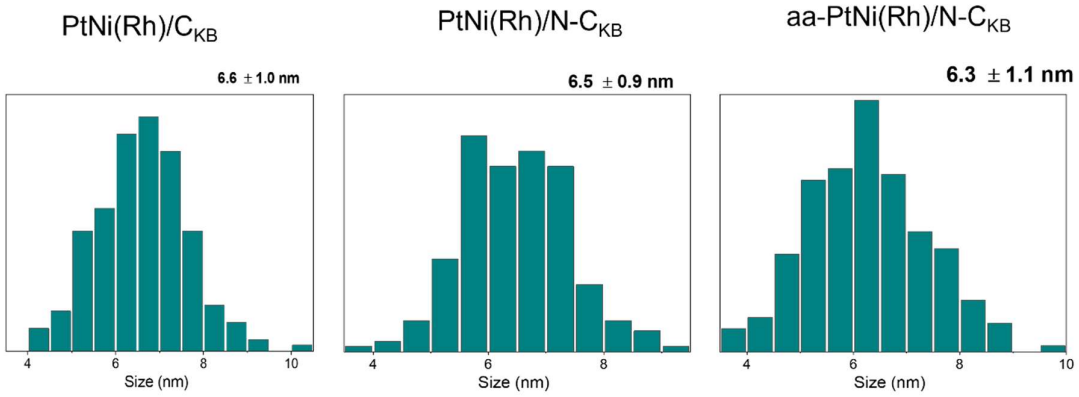

Fig. S20: Size analysis of TEM images for a) scaled-up 30 Pt wt% Pt_2Ni_1(Rh) onto C_{KB}, b) N-Doped C_{KB} and c) N-Doped C_{KB} after annealing and acid wash (aa).

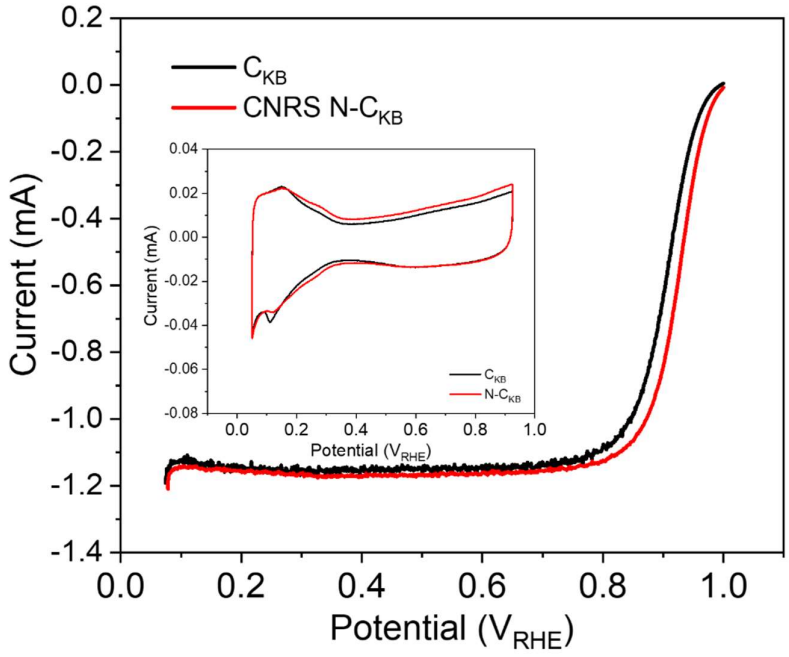

Fig. S21: CV and LSV of Annealed/leached "aa" scaled-up batches of oh-PtNi(Rh) catalysts.

Table S14. ECSA and MA of annealed/leached "aa"- scaled-up oh-PtNi(Rh) catalysts.

	$ECSA_{Hupd}$ ($m^2 g_{Pt}^{-1}$)	MA@0.9 V_{RHE} (A mg_{Pt}^{-1})	$ECSA_{CO}$ ($m^2 g_{Pt}^{-1}$)
Undoped C_{KB}	35.3 ± 4.3	0.67 ± 0.17	49.0 ± 4.7
N-C_{KB}	42.3 ± 1.2	1.42 ± 0.22	53.0 ± 3.2
Annealed leached undoped C_{KB}	37.0 ± 1.5	0.56 ± 0.05	47.7 ± 0.6
Annealed leached N-C_{KB}	37.0 ± 2.3	0.78 ± 0.34	47.7 ± 2.2

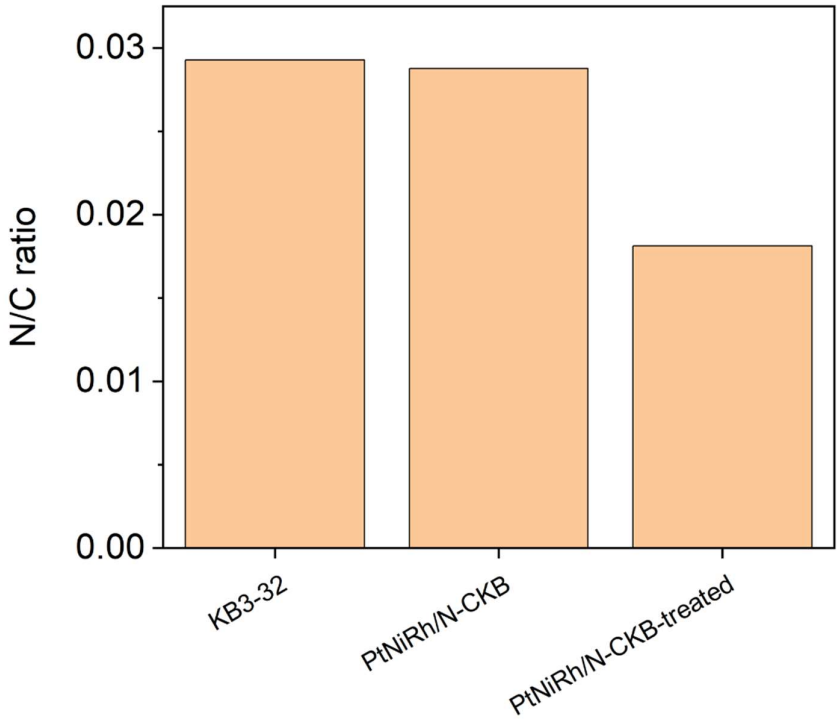

Fig. S22: Comparison of samples with N content in the carbon (ratio of wt%), upscaled, and after annealing and acid-leaching of the upscaled oh-PtNi(Rh) on N-CKB.

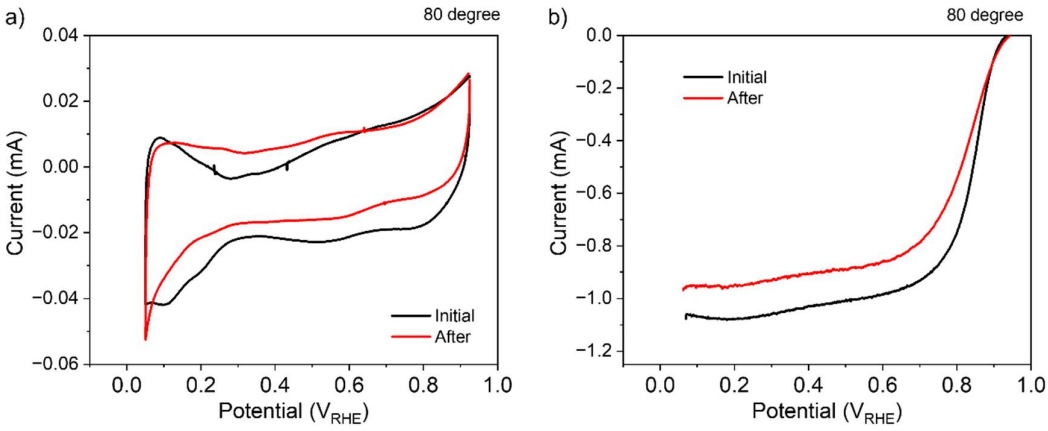

Figure S23: CV and LSV before and after 10k cycles AST under 80 °C of annealed/leached “aa” – scaled-up oh PtNi(Rh) catalyst.

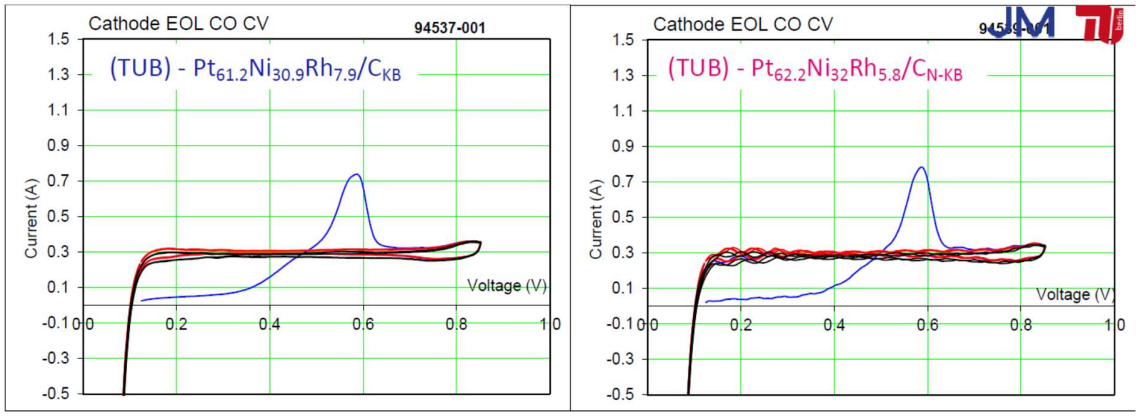

Fig S24: CO-ECSA in MEA, 100% RH.

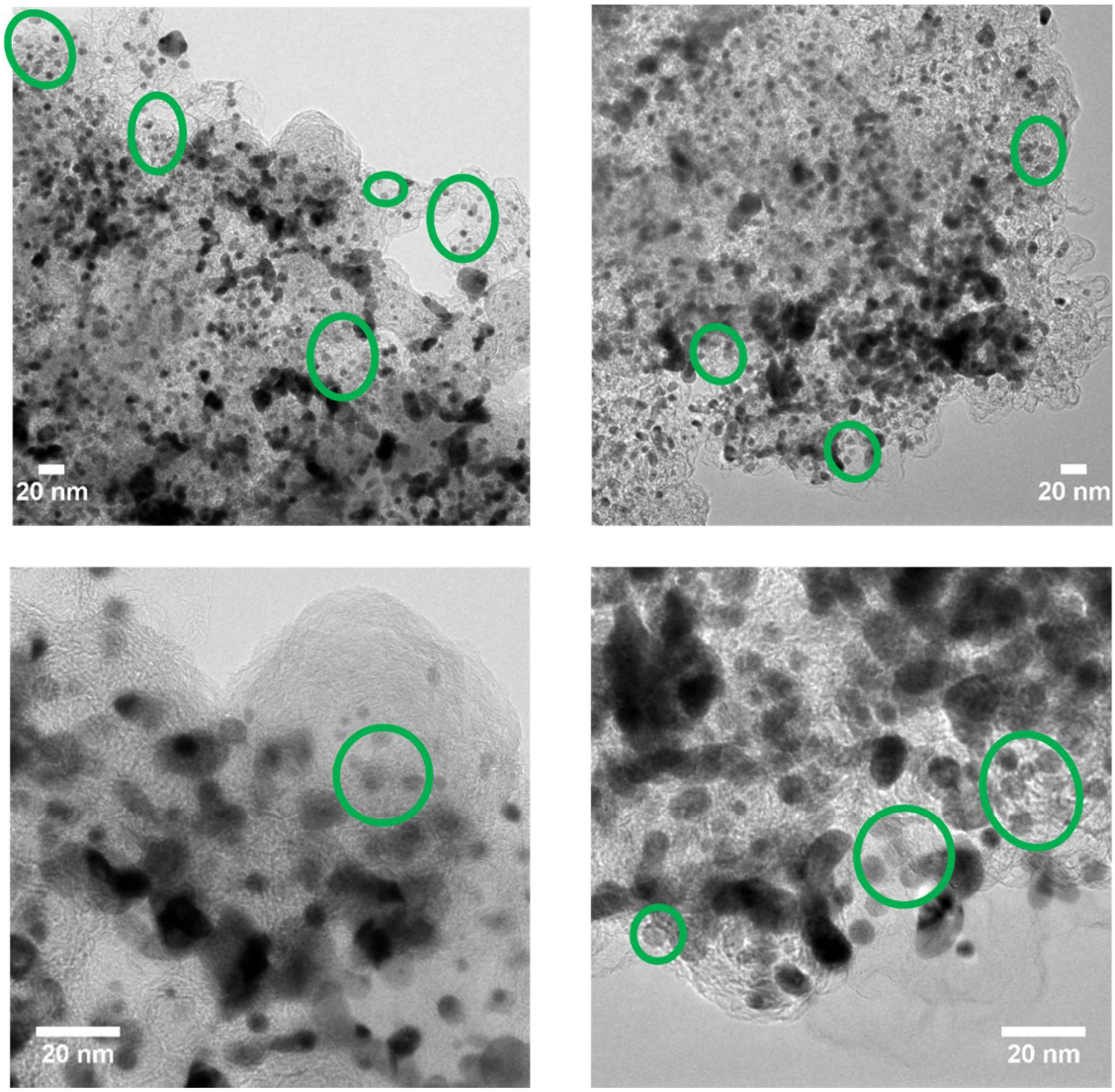

Fig. S25: TEM images of the annealed/leached upscaled oh-PtNi(Rh) catalyst on N-doped support after MEA test. Green circles for sustained octahedral nanoparticles.

Table S15. Membrane resistance during 100%RH polarization curves in O_2.

CCM cathode catalyst	Resistance / Ω cm^2
50%Pt/C2	0.041
PtNiRh/C(KB)	0.058
PtNiRh/(N-C(KB))	0.052

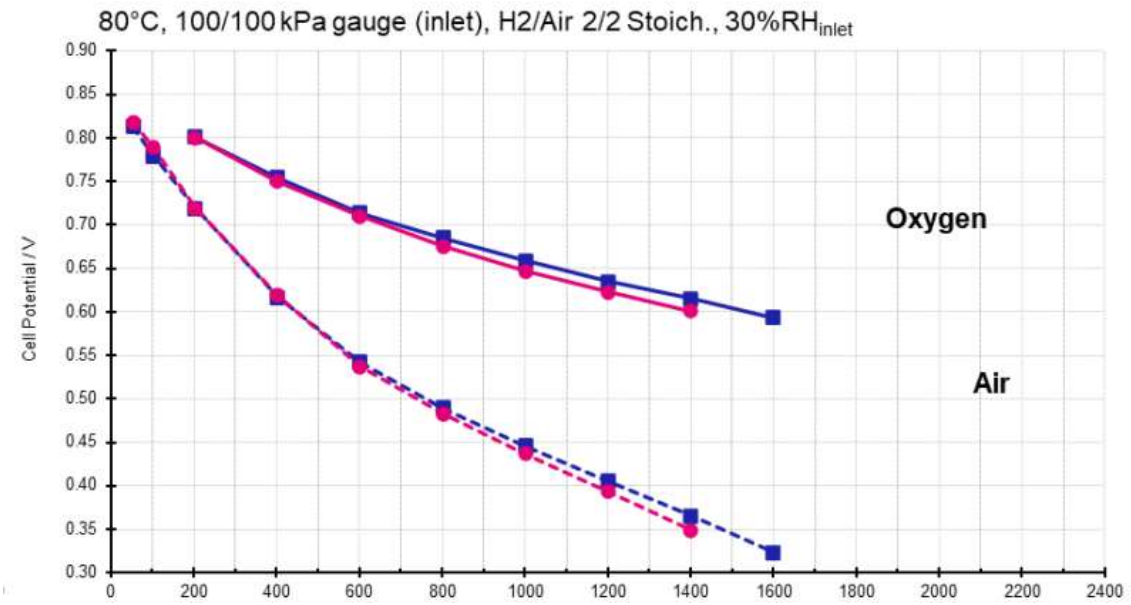

Figure S26. Comparison of N doping effect in MEA under 30 RH%. MEA single-cell performance of oh-PtNi(Rh)/C_{KB} (blue), N-doped oh-PtNi(Rh)/C_{KB} (red) as the cathode and Pt/C as the anode in H_2/O_2 (solid lines) and H_2/air (dashed lines). Polarization curves as a function of current density. The cathode loadings of oh-PtNi(Rh)/C_{KB} and N-doped oh-PtNi(Rh)/C_{KB} were 0.1 mg_{Pt} cm^{-2}, the loading for the anode was 0.1 mg_{Pt} cm^{-2}. Other test details are shown in the Fig. 6 in main.

References

1. Huang, X.; Zhao, Z.; Cao, L.; Chen, Y.; Zhu, E.; Lin, Z.; Li, M.; Yan, A.; Zettl, A.; Wang, Y. M.; Duan, X.; Mueller, T.; Huang, Y., High-performance transition metal–doped Pt3Ni octahedra for oxygen reduction reaction. *Science* **2015,** *348* (6240), 1230-4.
2. Dionigi, F.; Weber, C. C.; Primbs, M.; Gocyla, M.; Bonastre, A. M.; Spori, C.; Schmies, H.; Hornberger, E.; Kuhl, S.; Drnec, J.; Heggen, M.; Sharman, J.; Dunin-Borkowski, R. E.; Strasser, P.,

Controlling Near-Surface Ni Composition in Octahedral PtNi(Mo) Nanoparticles by Mo Doping for a Highly Active Oxygen Reduction Reaction Catalyst. *Nano Lett* **2019,** *19* (10), 6876-6885.
3. Ravel, B.; Newville, M., ATHENA, ARTEMIS, HEPHAESTUS: data analysis for X-ray absorption spectroscopy using IFEFFIT. *J Synchrotron Radiat* **2005,** *12* (Pt 4), 537-41.
4. Cui, C.; Gan, L.; Heggen, M.; Rudi, S.; Strasser, P., Compositional segregation in shaped Pt alloy nanoparticles and their structural behaviour during electrocatalysis. *Nat Mater* **2013,** *12* (8), 765-71.
5. Kocha, S. S., Principles of MEA preparation. In *Handbook of Fuel Cells*, Wolf Vielstich, H. A. G., Arnold Lamm and Harumi Yokokawa, Ed. John Wiley & Sons, Ltd.: 2010.
6. López-Cudero, A.; Solla-Gullón, J.; Herrero, E.; Aldaz, A.; Feliu, J. M., CO electrooxidation on carbon supported platinum nanoparticles: Effect of aggregation. *Journal of Electroanalytical Chemistry* **2010,** *644* (2), 117-126.